AD-A063 814 NAVAL RESEARCH LAB WASHINGTON D C F/G 20/5
LASER-PLASMA INTERACTION AND ABLATIVE ACCELERATION OF THIN FOIL--ETC(U)
DEC 78
UNCLASSIFIED NRL-MR-3890 NL

| OF |
AD
A063 814

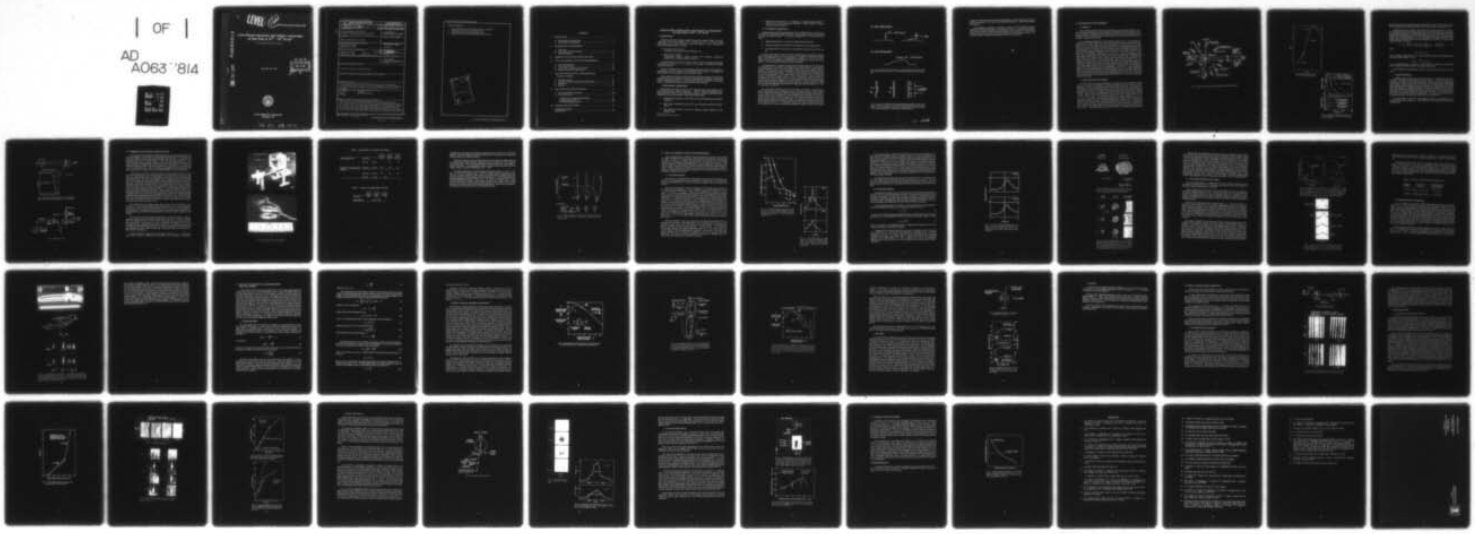

END
DATE
FILMED
3-79
DDC

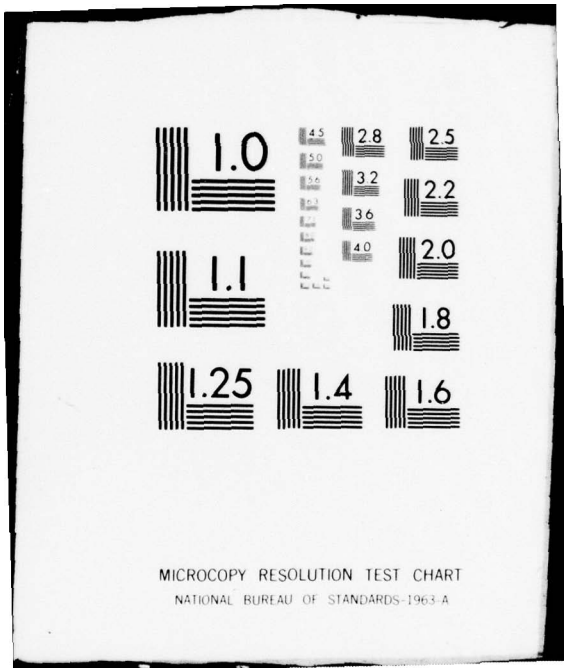
1.0
1.1
1.25
1.4
1.6
1.8
2.0
2.2
2.5
2.8
3.2
3.6
4.0
4.5
5.0
5.6
MICROCOPY RESOLUTION TEST CHART
NATIONAL BUREAU OF STANDARDS-1963-A

NRL Memorandum Report 3890

Laser-Plasma Interaction and Ablative Acceleration of Thin Foils at $10^{12} - 10^{14}$ W/cm^2

NRL Laser-Plasma Interaction Group

December 29, 1978

NAVAL RESEARCH LABORATORY
Washington, D.C.

SECURITY CLASSIFICATION OF THIS PAGE *(When Data Entered)*

REPORT DOCUMENTATION PAGE

READ INSTRUCTIONS BEFORE COMPLETING FORM

1. REPORT NUMBER: NRL MEMORANDUM REPORT 3890	2. GOVT ACCESSION NO.
3. RECIPIENT'S CATALOG NUMBER: NRL-MR-3890	
4. TITLE *(and Subtitle)*: Laser-Plasma Interaction and Ablative Acceleration of Thin Foils at 10^{12} -10^{14} W/cm^2.	5. TYPE OF REPORT & PERIOD COVERED: CONTINUING
	6. PERFORMING ORG. REPORT NUMBER
7. AUTHOR(s): NRL Laser Plasma Interaction Group*	8. CONTRACT OR GRANT NUMBER(s)
9. PERFORMING ORGANIZATION NAME AND ADDRESS: Naval Research Laboratory, Washington, D.C. 20375	10. PROGRAM ELEMENT, PROJECT, TASK AREA & WORK UNIT NUMBERS: 67H02-29A
11. CONTROLLING OFFICE NAME AND ADDRESS: Department of Energy, Washington, D.C. 20545	12. REPORT DATE: December 29, 1978
	13. NUMBER OF PAGES: 52
14. MONITORING AGENCY NAME & ADDRESS *(If different from Controlling Office)*	15. SECURITY CLASS. *(of this report)*: UNCLASSIFIED
	15a. DECLASSIFICATION/DOWNGRADING SCHEDULE

16. DISTRIBUTION STATEMENT *(of this Report)*

Approved for public release; distribution unlimited.

17. DISTRIBUTION STATEMENT *(of the abstract entered in Block 20, if different from Report)*

18. SUPPLEMENTARY NOTES

*NRL Laser-Plasma Interaction Group, B.H. Ripin, Code 6732, editor; C.M. Armstrong, † S.E. Bodner, R.Decoste, ‡ S.H. Gold,** J. Grun,††, R.H. Lehmberg, E.A. McLean, J.M. McMahon, D.J. Nagel, S.P. Obenschain, ‡ B.H. Ripin, J.A. Stamper, R.R. Whitlock, and F.C. Young (See reverse side)

19. KEY WORDS *(Continue on reverse side if necessary and identify by block number)*

Laser Fusion
Ablation
Acceleration
Absorption
Laser-Plasma Interaction

20. ABSTRACT *(Continue on reverse side if necessary and identify by block number)*

The interaction physics and hydrodynamic motion of thin-foil targets irradiated by long, low-flux Nd-laser pulses (3 nsec, 10^{12} -7 X 10^{14} W/cm^2) are studied experimentally and compared with theoretical models. Laser light absorption is high (80-90%) and thin-foil targets are accelerated up to ~ 10^7 cm/sec with good (~ 20%) hydrodynamic efficiency in the 10^{12}-10^{13} W/cm^2 range. These results agree with a simple rocket ablation model. Details of thermal heat flow both axially (related to ablation depth) and laterally (related to beam uniformity requirements) are also presented.

DD FORM 1 JAN 73 1473 EDITION OF 1 NOV 65 IS OBSOLETE
S/N 0102-014-6601

SECURITY CLASSIFICATION OF THIS PAGE *(When Data Entered)*

251 950

ITEM 18 CONTINUED

† Physics Department, North Carolina State University, Raleigh, NC
‡ Sachs/Freeman Associates, Inc., Bladensburg, MD
** National Research Council Resident Research Assoc.
†† Physics Department, University of Maryland, College Park, MD

CONTENTS

I. INTRODUCTION 1

A. High-Irradiance Coupling Physics 1
B. Low-Irradiance Coupling Physics 2

II. DESCRIPTION OF THE EXPERIMENT 5

A. Target Area 5
B. Laser System and Focal Conditions 5
C. Optical Probing Beam 8

III. ABSORPTION AND PARTICLE ENERGY BALANCE 10

IV. X-RAY AND THERMAL CONDUCTION MEASUREMENTS 15

A. X-ray Emission Spectra 15
B. Lateral Heat Conduction 17
C. Axial Thermal Conduction into the Targets 20
D. Spatially Resolved X-UV Spectroscopy 22

V. ABLATIVE ACCELERATION OF LASER-IRRADIATED THIN-FOIL TARGETS 25

A. Hydrodynamic Model 25
B. Abalation, Acceleration and Efficiency Measurements 27
C. Edge Effects 31
D. Summary 33

VI. FRONT AND REAR SURFACE BEHAVIOR 34

A. Front Surface Plasma Development 34
B. Rear Surface Motion 36

1. Interferometry and Shadowgraphy Methods 36
2. Reflected Light Methods 40
3. Streak Shadowgraphy Method 43

VII. SUMMARY AND CONCLUSIONS 45

ACKNOWLEDGMENTS 45
REFERENCES 47

LASER-PLASMA INTERACTION AND ABLATIVE ACCELERATION OF THIN FOILS AT $10^{12} - 10^{14}$ W/cm^2

I. INTRODUCTION

There has been a recent change in emphasis in laser fusion research at NRL.[1] Our current experiments are now at lower irradiance ($10^{12} - 10^{14}$ W/cm^2 versus $10^{15} - 10^{17}$ W/cm^2), longer pulse lengths (3 nsec versus 30-250 psec), with thin-foil targets (1 - 50 μm). The physics of these new experiments falls into two areas:

- *Laser-plasma interaction physics*
  (Absorption, heat transport, electron distribution, etc.)

- *Ablative acceleration physics*
  (Hydrodynamic efficiency, ablation pressure, laser uniformity requirements, Rayleigh-Taylor instability, adiabaticity, spall, etc.)

These experiments are the first in a series, in which we hope to accelerate a planar target to implosion-level velocities ($\sim 2 \times 10^7$ cm/sec),[2] and to evaluate, as completely as possible, the physics listed above.

Instead of imploding a pellet, we are accelerating a disk target, which can be thought of as approximating a section of a sphere (until convergence effects dominate). Disk targets have the advantage that one can diagnose the cold rear (inner) surface.

These experiments represent a break from previous NRL physics studies. This break was partially motivated by our interest in the physics of hydrodynamic acceleration, an area nearly devoid of experimental study so far.[3-7] This change was also made to escape from the growing number of undesirable side-effects of high-intensity laser-plasma coupling.

A. High Irradiance Coupling Physics:

Highly shaped laser pulses, in which a short high-peak-intensity spike irradiates a pre-formed plasma setup by a prepulse (simulating the effect of a long multi-nanosecond foot), such as illustrated in Figure 1a,[8] have been shown to produce a number of side effects that are undesirable for laser fusion application. These physics effects include:

- Reduction of the absorption of laser light due to the stimulated Brillouin backscatter instability.[9,10]

- High electron temperatures (tens-of-keV), that can preheat the pellet fuel prematurely.[11-13]

- High energy ion blowoff,[14] that does not efficiently transfer momentum to the imploding target.

Manuscript submitted December 19, 1978.

- Inhibited thermal conductivity,[11,12] probably due to megagauss magnetic fields,[15,16] which not only reduces hydrodynamic efficiency, but also increases the symmetry requirements of the irradiation.[17]

B. **Low-Irradiance Coupling Physics**:

Using laser pulses with lower peak irradiance, such as illustrated in Fig. 1b, will reduce or eliminate most of the undesirable effects listed above. Pellet designs have been proposed which use solely low-irradiance pulses.[18,2] At this lower irradiance ($10^{12} - 10^{13}$ W/cm^2) we have found:

- Efficient light absorption with reduced or neglible Brillouin backscatter.
- Cool electron distributions (250-400 eV) which should not cause preheat effects.
- Low energy ablative ion blowoff with a very efficient momentum transfer to the target.

For laser pellet implosion purposes, the lower irradiances imply longer pulses, in order to deliver the required energy. A most crucial question to be answered is whether the imploding shells will be sufficiently stable to the Rayleigh-Taylor instability,[19,20] and, if they are not, whether some of the suggestions for suppressing the Rayleigh-Taylor growth rate will be effective.[21] These points will be addressed in future experiments.

As mentioned earlier, the planar interaction geometry approximates that of a small section of a large pellet and has, in addition, great diagnostic and theoretical simplicity. The situation is shown schematically in Fig. 2. First, the interaction physics near the light absorption region is addressed. The absorption fraction is obtained by several scattered light diagnostics and by direct particle blowoff measurements. The character of the absorbed energy is examined with various x-ray measurements. These include both UV-spectral, Bremsstrahlung, time-resolved and space-resolved measurements. There is a study of the speed and depth of penetration of the thermal wave into the target interior, and of the lateral thermal conductivity relating to incident beam uniformity requirements. Axial and lateral heat transport is examined utilizing layered targets[22] and spatially modulated focal spots respectively. We also present here the total light and particle blowoff angular distributions and energy and momentum balance at 3×10^{12}, 1×10^{13}, and 7×10^{14} W/cm^2.

Next, the ablative acceleration of the thin foil targets is considered. A simple "rocket" ablation model describing the hydrodynamic motion of the target is derived and is compared with the experimental hydrodynamic efficiency, ablated mass loss and ablation velocity, and target recoil velocity, with good agreement. The rear surface motion and behavior of the foil are studied by several means. Both time-integrated and time-resolved measurements provide information on the foil's speed, shape and physical state. It is found that the motion of this surface appears ablatively accelerated and does not appear to be dominated by shockwave characteristics such as spallation, fluff, etc..[23] The dominant features of the material accelerated away from the laser agree with a simple one-dimensional hydrodynamic ablation model (rocket model)

(a) HIGH IRRADIANCE

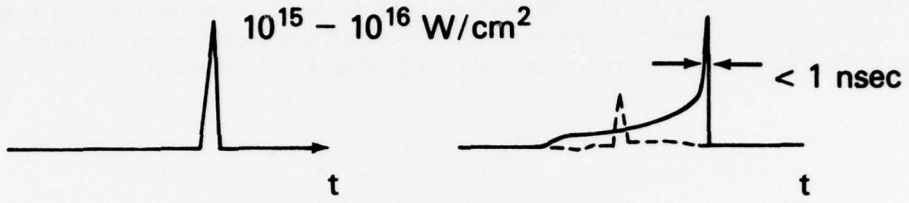

(b) LOW IRRADIANCE

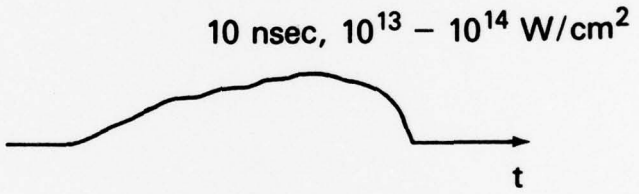

Fig. 1 — Basic laser pulse shapes for laser fusion. (a) Short high-irradiance laser pulses used and proposed in earlier laser fusion research. (b) Longer lower-irradiance laser pulse used in these studies.

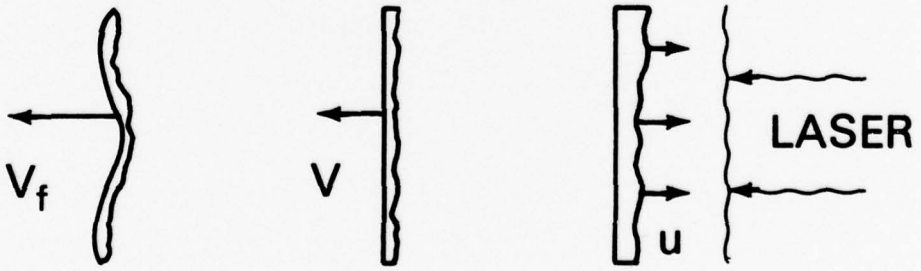

Fig. 2 — Aspects of the acceleration of thin targets by laser-induced ablation. The laser light is absorbed near the critical density and heat flows to the ablation surface where ions blowoff with velocity u. The target accelerates to velocity v due to the momentum imparted by the ablation. Finally, hydrodynamic instability may warp the target at some final velocity v_f.

modified to include some two-dimensional expansion effects. Ablative acceleration of cold target foils up to speeds of 10^7 cm/sec with hydrodynamic efficiency of $\sim$20% are demonstrated experimentally.[1]

The experimental arrangement is described in Section II. The experimental results of absorption and particle energy balance are presented in Section III, x-ray and thermal conductivity results in Section IV, ablation and foil acceleration studies in Section V, and both front surface and rear surface behavior are described in Section VI as measured by a number of optical means. Finally, a summary and conclusions are presented in Section VII.

II. DESCRIPTION OF THE EXPERIMENT

A. Target area:

Planar irradiation geometry has been chosen because of its good approximation to a section of a large thin-shell pellet, the good experimental accessability of the rear (inside) surface, and the simplicity of interpretation. We operate with as large a ratio of focal-diameter-to foil-thickness as possible (consistent with the required irradiance) to minimize both edge effects and irradiance variations across the target.

The experimental arrangement for these studies is shown in Fig. 3. Thin foil targets are mounted on an adjustable ladder in the center of the target chamber near the focal region of an aspheric f/10, 1-m focal length lens. For these experiments the target normal is usually oriented 6° from the beam axis so that specular reflection can be distinguished from backscatter and so that the axis of symmetry of the ion blowoff is more experimentally accessible. The focal distribution in the real target plane is cross-checked on each shot with an equivalent focal plane lens.[24] The irradiance is adjusted to be 3×10^{12} W/cm^2, 1×10^{13} W/ cm^2, or 7×10^{14} W/cm^2 in the experiments to be discussed. That fraction of incident and backreflected light which reflects off one surface of an optical flat is sent into calorimeters, fast (~300 psec) PIN optical diodes and imaging vidicons. Light and particle energy angular distributions are obtained with paired arrays of (16) minicalorimeters placed around the target[9,10]. Particle energy measurements on the back side of the target yield the hydrodynamic efficiency of acceleration. Angular distributions of ion ablation and target recoil velocities are obtained with time-of-flight charged particle collectors also distributed around the target. Several additional velocity and density diagnostics such as shadowgraphy, interferometry, streak photography, Doppler velocity sounding methods and ballistic pendulum are used. All these experimental results are cross-checked for consistency. X-ray diagnostics and UV (40 eV-400 eV) spectra are used to study thermal conductivity and electron energy distributions in the target. These diagnostics and others used for these experiments will be described in more detail in the appropriate sections of this report.

B. Laser System and Focal Conditions:

The laser system used for these experiments is a modified version of the Pharos II system which has been previously described.[25] The major modifications for these experiments are the following: 1. *Oscillator*: The subnanosecond mode-locked Nd:Yag oscillator was replaced by a Quantel passively Q-switched Nd:Yag oscillator. This oscillator operates in a single longitudinal and transverse mode and can produce unmodulated pulses three nanoseconds in duration (FWHM). Three successive rod amplifiers are used to obtain a beam energy of about 20 Joules on target. Figure 4 shows the temporal shape of the laser pulse over several decades in irradiance. 2. *Target Location*: For the present experiments, average irradiances of 3×10^{12}, 1×10^{13} and 7×10^{14} W/cm^2 are obtained by placing the target at different locations between the lens and the minimum focal spot. These focal distributions are shown in Fig. 5. The system is aligned to obtain the best smooth and reproducible pattern in the target plane. The beam quality is in general quite good, and at best focus half of the energy is contained in 70μrad cone angle. However, the spatial uniformity of the focal patterns in the target plane is marginal, as seen in Fig. 5. Some astigmatism is present, which marred the azimuthal symmetry, and the

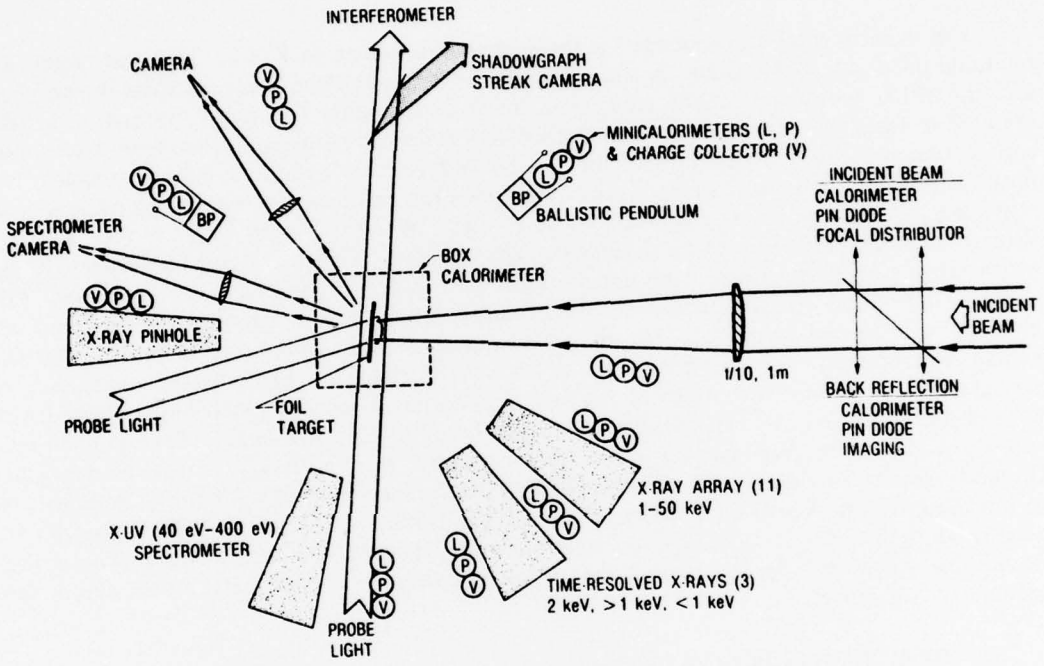

Fig. 3 — Schematic of the experimental apparatus, diagnostics and irradiation geometry.

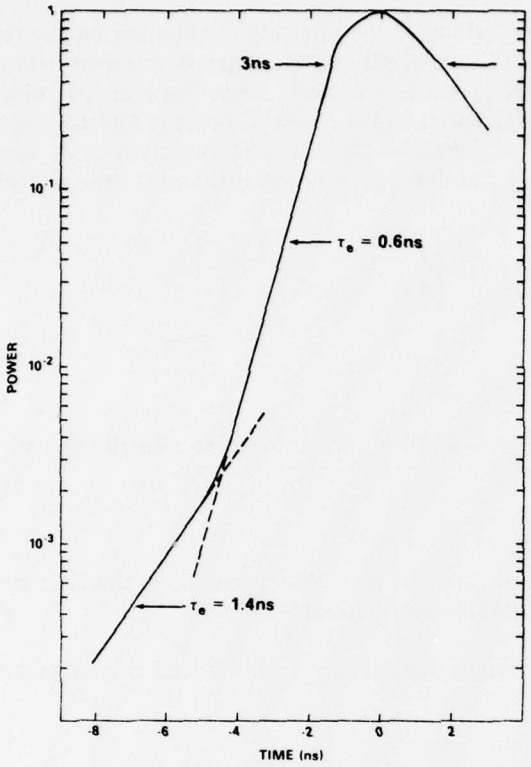

Fig. 4 — Temporal shape of the incident Nd-laser pulse in these experiments.

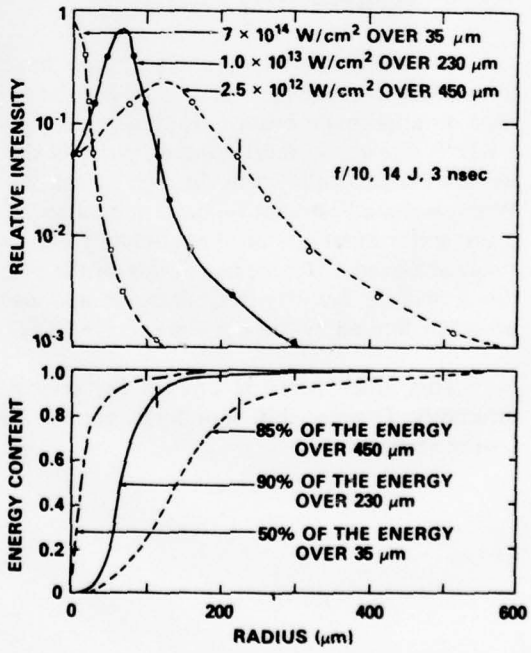

Fig. 5 — Radial laser intensity and energy content profiles at the target. These profiles are averaged over the azimuthal angle.

beam intensity does not monotonicaly decrease from center to edge. Focal distribution measurements indicate that the peak-to-valley ratios in the center lobe vary from about 3:1 to 10:1.

Calculations show that, ultimately, the uniformity of the intensity distribution on the target can be made as good as the laser near-field pattern by placing the target in the near-field of the focusing lens (out-of-focus). This technique produces a uniform large-diameter spot which is desirable for hydrodynamic acceleration to high speed and is essential to study hydrodynamic stability. The intensity distribution $I'(r', Z_o)$ in the target plane located at a distance Z_o from the focal plane for incident intensity and phase distributions $I(r)$ and $\beta(r)$ on a lens of focal length f and radius a is given by

$$I'(r', Z_o) = C\left|\int_o^a \epsilon(r) J_o\left[\frac{krr'}{f - Z_o}\right] \exp\left[i\left(\frac{1}{f - Z_o} - \frac{1}{f}\right)\frac{kr^2}{2}\right] r\, dr\right|^2, \qquad (1)$$

where

$$\epsilon(r) = I(r)^{\frac{1}{2}}\, e^{i\beta(r)},$$

and C is a constant. Figure 6 shows $I'(r', Z_o)$ for a uniform incident intensity distribution with a soft edge at the lens radius a; i.e., for

$$I(r) = e^{-\left(\frac{r}{0.87a}\right)^{14}}, \quad \beta(r) = 1$$

at Z_o = 5.5 mm and for an a = 10 cm, f = 120 cm (f/6) lens. Modifications to the laser system are presently being made to achieve such uniform distributions.

Some indications of minimum beam uniformity requirements will be shown later in this report.

C. **Optical Probing Beam**:

A different optical probing system has been constructed to investigate the laser-matter interaction. A schematic of this arrangement is shown in Fig. 7. A portion of the 1.06 μm, 3 nsec duration main beam is split off near the oscillator, amplified and frequency-doubled using a KD*P crystal. A short duration pulse is sliced from the 5320 Å output of the crystal doubler using a Pockels cell driven through its full wave voltage by a laser triggered spark gap (LTSG). With careful adjustment of angle and amplitude of the triggering pulse going into the spark gap, probe pulse durations of approximately 400 psec and time jitter of $\pm$0.5 nsec have been routinely achieved. The precise timing of the probing pulse with respect to the main pulse is monitored with a fast-rise-time detector and oscilloscope. The duration of the probe pulse is presently limited by the rise-time of the LTSG which drives the Pockel's cell.

This probe beam is utilized for several diagnostic purposes, e.g., shadowgraphy, interferometry, Doppler shift soundings, etc. These applications will be discussed further in the following sections.

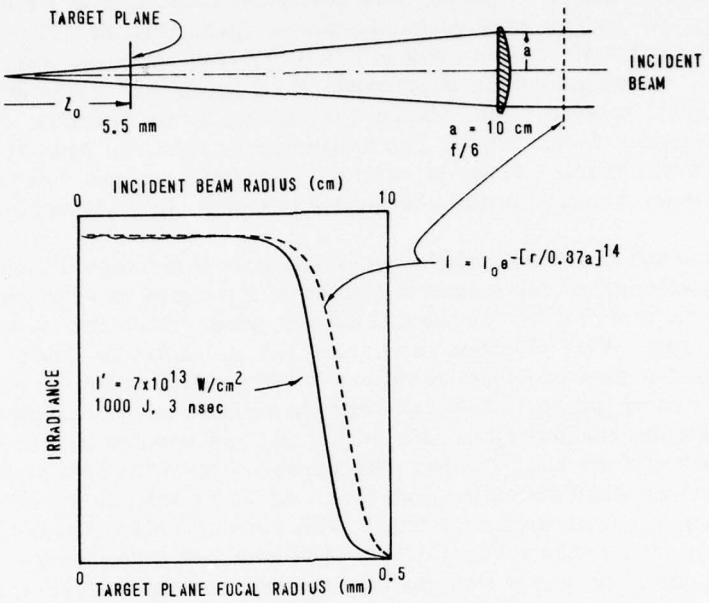

Fig. 6 — A uniform tailored beam distribution $I(r)$ in the lens plane and the predicted uniform focal distribution $I'(r')$ in the near field.

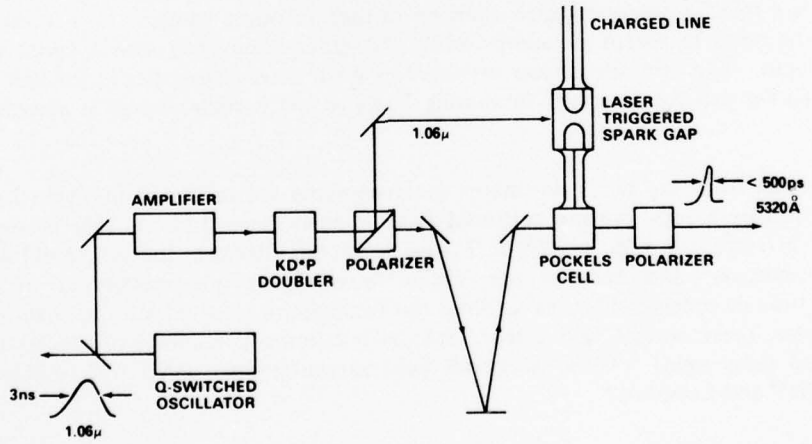

Fig. 7 — Optical probe system.

III. ABSORPTION AND PARTICLE ENERGY BALANCE

In this section we will describe the various measurements of the laser light absorption by the thin-foil plasmas. Scattered light and total absorption measurements are made using a box calorimeter (Fig. 8a) and an array of minicalorimeter pairs (Fig. 8b). It is found that the absorption is 90% at 3×10^{12} W/cm^2, 80% at 1×10^{13} W/cm^2 and higher than 50% at 7×10^{14} W/cm^2 and good energy accounting is achieved. With our present instrumentation, the total measured energy of scattered light, plasma blowoff and x-rays emission, etc. balances the incident laser energy to within $\pm 10\%$. The measurements presented here are made using 10-μm to 15-μm thick CH foils. However, absorption measurements did not significantly differ from these values for Al targets or for other thicknesses sufficient to prevent burnthrough.

The construction of the box calorimeter is similar to that designed by S. Gunn.[26] Each side of the box calorimeter has a panel composed of filter glass (on the inside of the box) which is in thermal contact with a Cu thermal diffuser, whose temperature is measured by solid state Peltier sensors. The NRL box calorimeter has its calibration heater wire imbedded between the absorber glass and thermal diffuser to better approximate the heat deposition in actual use. Each panel is calibrated optically with the incident beam calorimeter. The focused laser beam enters the box through a hole in one end and impinges on the target, which is located at the center of the box. The box then absorbs all the energy given off by the plasma, except that which escapes through the lens cone ($\pm 3°$). In order to shield the panels from ions, a pyrex cube is placed around the target. This ion shield also stops UV and soft x-rays. Especially in large f/no. systems, which have a small lens cone angle, the ion shield intercepts appreciable amounts of ion energy from the irradiated target, which it slowly radiates thermally, causing the energy measured by the box calorimeter to increase with time. This observed drift agrees well with a calculation based on Stefan's law and the thermal constants of the ion shield. This thermal contribution due to the ion shield has a different time constant than the optical contribution and is easily corrected for in use.

The minicalorimeters are arranged in pairs about the target. The active element in each calorimeter is a thin Ta absorbing disk attached to thermocouple wires.[27] One minicalorimeter in each pair is open to accept all energy while the other is covered with a pyrex window to accept only light. The minicalorimeter sensitivities were measured optically for light detection and calculated for particle detection (assuming 100% of the particle energy is absorbed on the Ta disk).

The results from the box calorimeter measurements are tabulated in Table I. The box calorimeter measurements indicate scattered light to have been $15\% \pm 10\%$ of the incident light at 10^{13} W/cm^2, and $47\% \pm 10\%$ at 7×10^{14} W/cm^2. Because the ion shield is used for these measurements, and because the visible wavelengths and harmonics of the laser wavelength, though considerably weaker than the fundamental, would still be absorbed by the box calorimeter, these energy figures represent the maximum percentage of the scattered light (non-absorbed laser light). These scattered light measurements agree with others made at NRL,[28] Sandia[29] and Lebedev.[3]

The light transmitted through the 15-μm CH targets is about 15% at 7×10^{14} W/cm^2 and about 1.5% at 10^{13} W/cm^2, as measured by the back panel of the box calorimeter. Presumably,

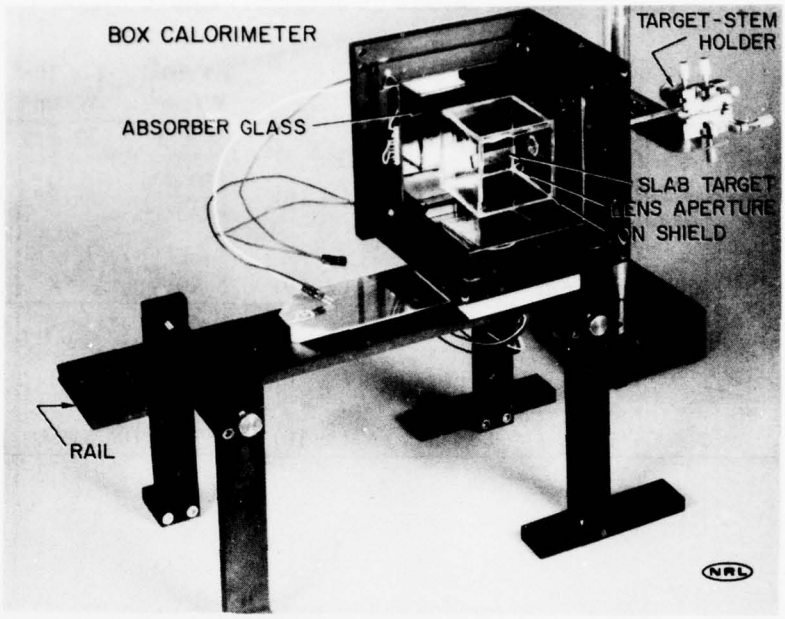

(a)

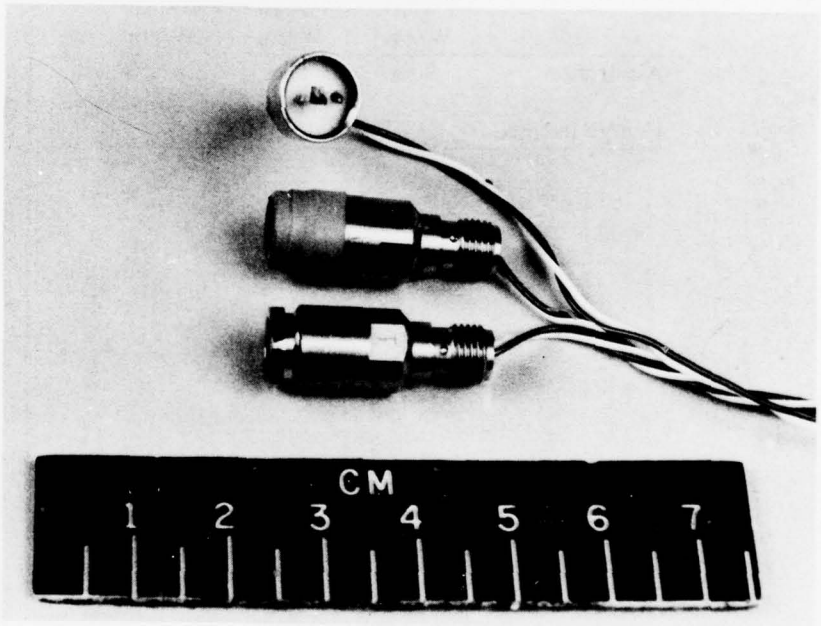

(b).

Fig. 8 — Scattered light and particle energy diagnostics.
(a) Box calorimeter. (b) Minicalorimeters.

Table I — Energy Balance (% of Incident Laser Energy)

			3×10^{12} W/cm^2	1×10^{13} W/cm^2	7×10^{14} W/cm^2
Scattered light (4π)	mini-cal's		9 ± 5	20 ± 5	44 ± 10
	box-cal	(± 10)	-	15	47
Particles, UV and x-rays (4π)	mini-cal's	(± 10)	90	78	52
TOTALS					
	mini-cal's	(± 10)	99	98	96
	box-cal	(± 10)		105	

Table II — Absorption and Energy Balance Summary

	3×10^{12} W/cm^2	1×10^{13} W/cm^2	7×10^{14} W/cm^2
Absorption	90%	80%	> 55%
Energy Balance		100 ± 10%	

this difference exists because the foil becomes underdense during the laser pulse at the higher irradiance. The exact thickness at which burnthrough occurs is dependent on the spatial and temporal profiles of the incident laser beam.

With the ion shield removed, one would expect the box calorimeter to measure nearly all of the absorbed laser energy, except for small contributions from backscatter (1%), ion blowoff into the lens cone ($< 1\%$), and energy absorbed by the target holder (which was designed to subtend a small angle). This measurement is made, and the box calorimeter receives all of the incident radiation, to within the experimental error ($\sim 10\%$).

The angular distributions of the scattered light and particle energy at 3×10^{12}, 1×10^{13} and 7×10^{14} W/cm^2 are shown in Fig. 9. These are obtained with the minicalorimeter array. Note that the particle distribution peaks normal to the target while the scattered light peaks both back towards the focusing lens and at the specular angle (12°).[28] The backscattered energy increased dramatically between 10^{13} W/cm^2 and 7×10^{14} W/cm^2, as noted previously,[30] due to the stimulated Brillouin instability. These angular distributions were integrated over all solid angles to yield the total scattered light and particle energies given in Table I. Note the good consistency of the light, particle and total energy measurements. Table II shows a summary of the absorption and energy balance at the three standard irradiances.

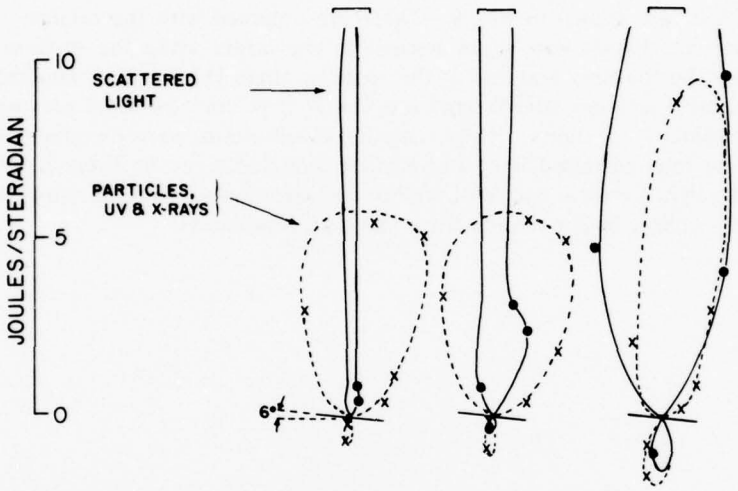

CONDITIONS

Joules incident		10.7	15.3	16.1
irradiance	W/cm^2	3×10^{12}	1×10^{13}	7×10^{14}
spot size	μm	450	230	35
CH target thickness, μm		10	16	16

Fig. 9 — Angular distributions of scattered light and particle blowoff at irradiances of 3×10^{12}, 1×10^{14} and 7×10^{13} W/cm^2. Laser light is incident vertically from the top.

IV. X-RAY AND THERMAL CONDUCTION MEASUREMENTS

X-ray measurements give information about the temperature distribution in the absorption region and target interior, and can give a good indication of the heat flow properties within the target. In Section A we discuss the measurement and interpretation of the spectrally resolved but time-integrated bremsstrahlung and of the time-resolved x-ray traces. Lateral thermal conductivity is examined in Section B and is related to spatial beam uniformity requirements for ablative acceleration studies. Section C reports the utilization of layered target techniques to obtain an estimate of the depth of axial heat flow into the target interior. Finally, in Section D, spatially-resolved XUV spectral measurements are presented which adds data on the temperature distribution in the target.

A. X-ray Emission Spectra:

Spectra of the x-ray emission from thin film targets are measured in the region from 1 to 10 keV. The bremsstrahlung continuum is determined by using an array of seven PIN diodes and filters as described in Ref. 31. The array is located at an angle of 120° to the incident laser direction.

Results for both polystyrene (CH) and aluminum (Al) foil targets are given in Fig. 10. For CH, an electron temperature of ~250 eV is deduced from the spectra below 3 keV at both 1×10^{13} W/cm^2 and 7×10^{14} W/cm^2. Above 3 keV, the enhanced x-ray emission for an irradiance of 7×10^{14} W/cm^2 suggests that non-thermal electrons are being generated in the laser-target interaction, probably by a parametric instability. This was also observed in other similar experiments.[32] For the present CH measurements, the integrated x-ray emission greater than 1 keV is 8 mJ at 1×10^{13} W/cm^2 and 5 mJ at 7×10^{14} W/cm^2 (based on isotropic angular distributions of x-ray emission) and therefore represent a negligible energy loss. The spectra for aluminum are not plotted below 2 keV because x-ray line emission from highly ionized Al ions occurs in this region and the filter-detector technique is unable to separate line emission from the continuum. At 10^{13} W/cm^2, the bremsstrahlung continuum from Al is about 100 times greater than that from CH but is of similar spectral shape. For Al, an electron temperature of ~400 eV is deduced from the spectra below 6 keV at both 1×10^{13} W/cm^2 and 7×10^{14} W/cm^2. The integrated x-ray emission (over 4π) greater than 2 keV is 40 mJ at 10^{13} W/cm^2 and 30 mJ at 7×10^{14} W/cm^2. The integrated x-ray emission above 1 keV is > 0.7 J at 10^{13} W/cm^2 and > 0.5 J at 7×10^{14} W/cm^2. This is based on the observed saturation of detectors below 2 keV.

The time dependence of the x-ray emission has been studied using detectors with subnanosecond time response. A PIN diode with 0.4 nsec rise and fall times is used with a 1 mil Be filter to measure 1-2 keV x-rays. The response of two such detectors — one recording the incident laser pulse and the other measuring x-rays — are shown in Fig. 11. In this case, the laser oscillator generated two adjacent longitudinal modes so that the incident laser pulse envelope showed strong nanosecond-duration modulation. The structure of the incident laser pulse is reflected in the x-ray PIN diode response for both CH and Al targets with some smoothing of the rapid time variations. Multimoding by the laser is infrequent, and is not present in the shots presented in the remainder of this paper.

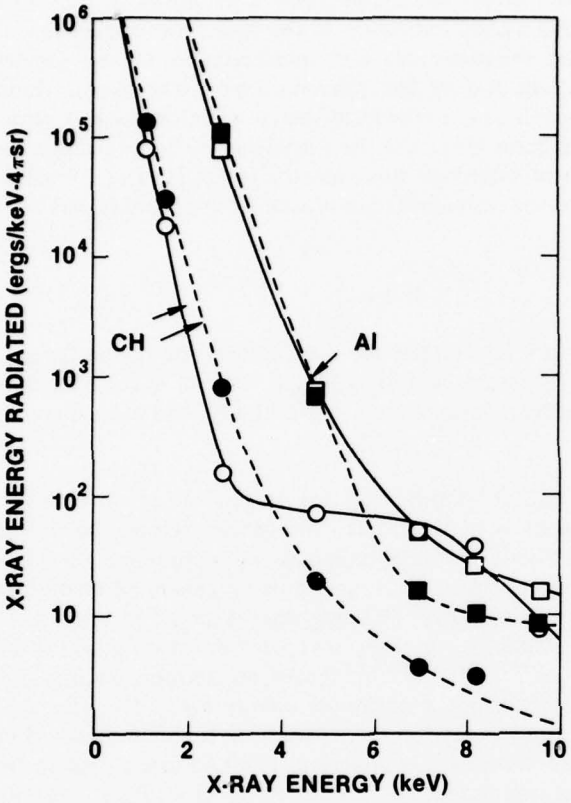

Fig. 10 — X-ray spectrum measured on CH (16-μm-thick) and Al (7.0-μm-thick) foil targets irradiated by 20-J, 3-nsec laser pulses. The spectra at 10^{13} W/cm^2 are indicated by solid data points (● ■), and at 7×10^{14} W/cm^2 by open data points (○ □).

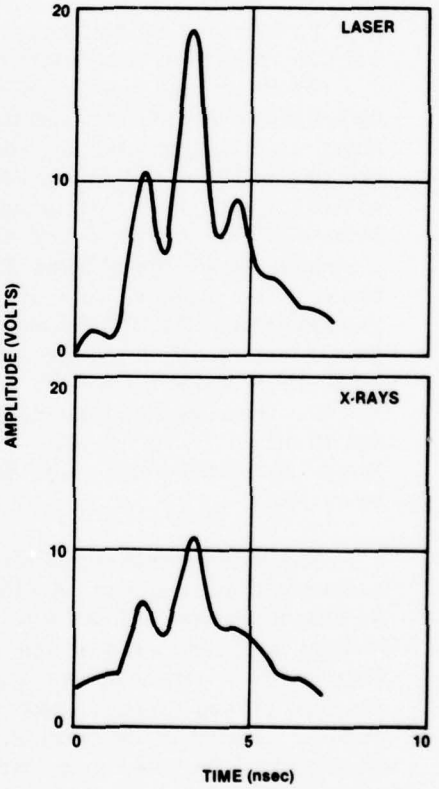

Fig. 11 — Time-resolved PIN x-ray diode response. Top: Incident pulse shape of 24-J laser pulse ($\sim 10^{13}$ W/cm^2) for a multimode oscillator pulse. Bottom: X-ray pulse (>1 keV) measured for a CH target irradiated with the laser pulse shown above.

The PIN diode detector is limited to measurements of low energy x-rays because the sensitive thickness of the detector is small. For higher energy x-rays, a 6.4-mm thick plastic scintillator (NE-111) quenched with 3% benzophenone is coupled to a coplanar photodiode to provide a subnanosecond x-ray detector. A combined detector-oscilloscope response of 0.6 nsec (FWHM) was measured with a 0.3-nsec incident laser pulse and a Tektronix oscilloscope (Model 519). This does not include the scintillator time response, which should be about 0.3 nsec (FWHM) as determined for similar scintillators.[33] The detector response to x-rays emitted from an Al target irradiated with a 19-J, 3-nsec pulse and transmitted through a 12.5-μm aluminized mylar filter is shown in Fig. 12. Here the shape of the x-ray pulse is compared with the incident laser pulse as measured by a photodiode and oscilloscope with subnanosecond time response. The time dependence of the x-ray signal is identical to that of the laser pulse to within experimental uncertainty.

For temporally smooth incident laser pulses, such as shown in Fig. 12, no modulation of the x-ray emission has been observed with either subnanosecond x-ray detector. For shots where the incident laser pulse was temporally modulated, such as shown in Fig. 11, both x-ray detectors record modulation of the x-ray emission with some smoothing of the rapid time variations.

B. Lateral Heat Conduction:

The lateral heat conduction rate is an important property of the laser-plasma interaction in two ways: first, as a heat loss mechanism, and second, as an effect which determines the spatial uniformity requirement of the laser beam for ablative acceleration. The lateral heat loss is important for interpretation of planar target experiments and will be discussed later in Section V on ablation studies. Knowledge of the laser uniformity specifications is essential to avoid driving the Rayleigh-Taylor instability and to provide sufficient spherical convergence.

For one-dimensional systems, the pressure P_a at the ablation surface can be expressed in terms of the absorbed laser irradiance I_a and front surface ablation velocity u, by

$$P_a = \frac{2I_a}{u}. \tag{2}$$

An upper limit on the ablative pressure differential ΔP that is allowable between two sections of a target, given a relative displacement Δr upon linear acceleration through a distance r, is given by

$$\Delta P \leqslant P_a \frac{\Delta r}{r}. \tag{3}$$

This is in the absence of hydrodynamic instability. Raleigh-Taylor instability may put a more stringent requirement on the pressure uniformity.

A suggestion that the lateral heat flow is low, at least in the region of 1 keV x-ray emission, is seen in Fig. 13. Here the laser focal distribution is compared with an x-ray pinhole photograph of the rear of a CH foil. Note that the hot spot details of the x-ray image correspond well to those in the incident beam.[34] "Classical" lateral heat flow of a significant fraction of the incident energy at $T \approx 250$ eV would result in only a 2% temperature differential 30 μm away from a hot spot. This is insufficient to yield the observed x-ray nonuniformities.

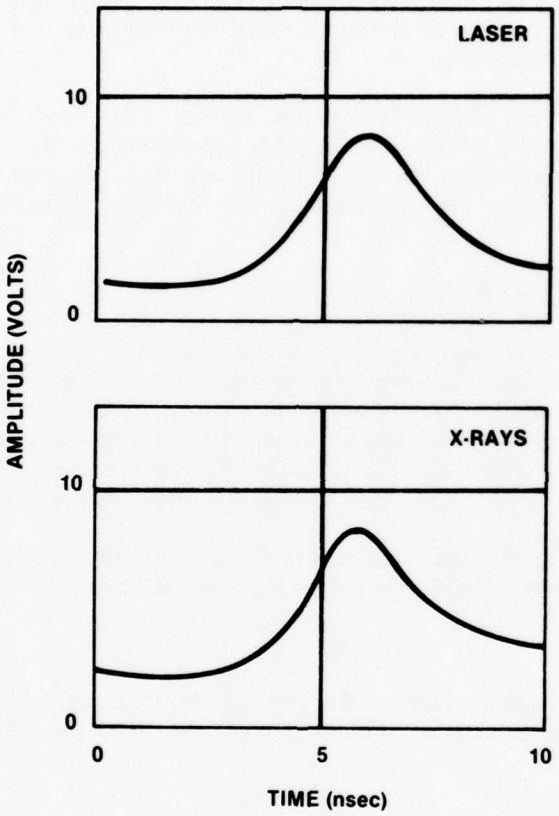

Fig. 12 — Time-resolved scintillator-photodiode x-ray detector results. Top: Incident pulse shape of 19 J laser pulse ($\sim 10^{13}$ W/cm^2). Bottom: X-ray pulse (> 5 keV) measured from an Al target irradiated with the laser pulse shown above.

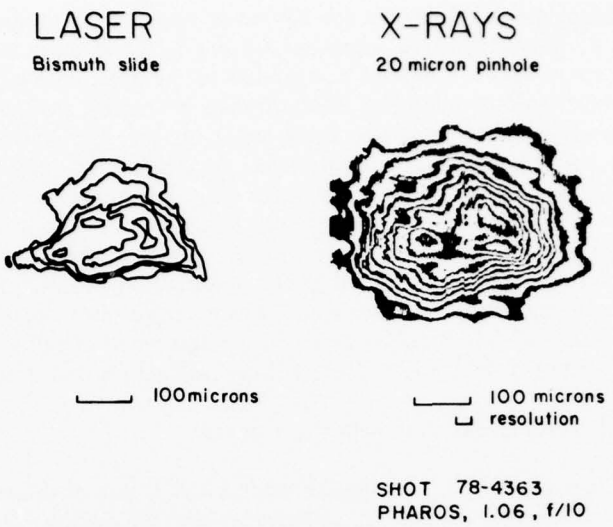

Fig. 13 — Retention of beam hot spots in the interaction region at 10^{13} W/cm^2. Left: Focal spot profile. Right: Isodensity contours of x-ray pinhole photo of rear of irradiated CH foil.

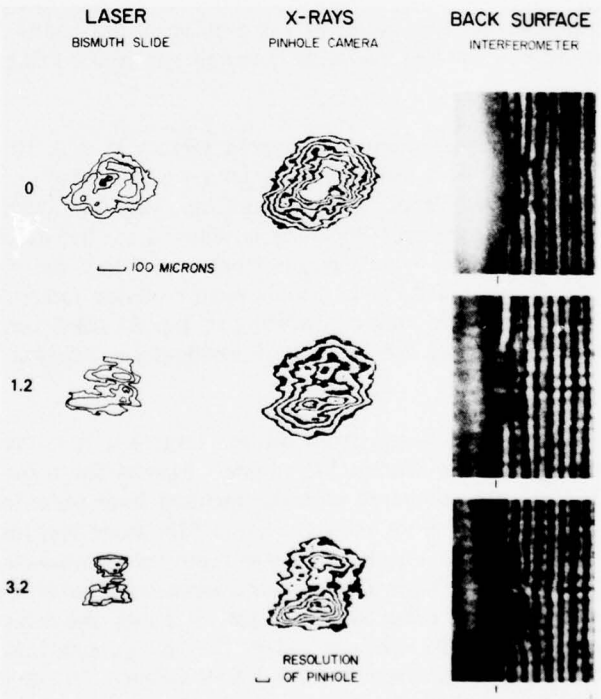

Fig. 14 — Beam non-uniformity effects. Left: Laser focal spot distribution. Middle: Isodensity contours of X-ray pinhole photo of target rear. Right: Protrusions on target rear surface seen via interferometry. Numbers on left are the widths (in cm) of strips, placed horizontally across lens (diameter of beam $\simeq$ 8 cm), used to produce the spatially modulated focal spot.

Although beam non-uniformities are obviously retained at, or slightly beyond the critical density surface, the most important region of concern is the ablation surface. Figure 14 shows that gross non-uniformities are indeed transmitted to the ablation surface and are not washed out. This is demonstrated by taking an interferogram of the foil during the shot to see whether bumps corresponding to hot spots are discernable on the rear surface as a result of non-uniformity at the ablation surface. Intensity lobes are deliberately introduced in the focal distribution by placing varying widths of an opaque strip across the center of the focusing lens (coded aperture). The effect of a factor of three intensity variation in the beam focal spot distribution is easily seen in the x-ray image and in corresponding bumps on the rear surface. Clearly this is not sufficiently uniform for pellet compression. Refinements of this coded aperture technique will be made to determine beam uniformity requirements and to study Rayleigh-Taylor instability. It is not known at this point whether self-generated magnetic fields or some other mechanism dominate the lateral heat conduction rate in this irradiance regime.[12]

C. **Axial Thermal Conduction into the Targets**:

The use of layered targets, i.e., targets made up of layers of different materials, has been previously used with good success[22] to determine heat conduction rates into the interior of laser-plasma targets for high intensity, short pulses.

Targets consisting of thin layers of CH on Al foil substrates are used to estimate the thickness of material ablated from a target. For these experiments, both x-ray spectral distributions and the temporal emission of x-rays are measured. Since the Al substrate is a more intense x-ray emitter than the CH overlayer (as previously indicated), a measure of the x-ray intensity as the thickness of the CH overlayer is varied can be used to estimate the thickness of the ablated material.

Results of spectral measurements of layered targets at 3×10^{12} and 10^{13} W/cm^2 are presented in Fig. 15. Ratios of x-ray intensities for layered targets to intensities measured on thick CH targets are displayed versus x-ray energy for different thicknesses of CH overlayer. These ratios increase as the overlayer thickness is reduced so that more of the Al substrate is heated. Detectors corresponding to data points from 1 to 3 keV are most sensitive to heating of the Al because highly-ionized Al is a copious source of line radiation in this energy range. For example, at 10^{13} W/cm^2 only minimal heating of the Al substrate is apparent for a 2-μm CH overlayer, and no heating of the substrate is evident for 3.5-μm, 4.0-μm and 5-μm CH overlayers.

The temporal emission of x-rays from layered targets is measured using the previously described fast time response, Be-filtered PIN diode. Results for three different targets at an irradiance of 10^{13} W/cm^2, are compared with the incident laser pulse in Fig. 16. These measurements are made on separate shots using the same PIN diode and oscilloscope. The oscilloscope time jitter is $\pm$ 0.25 nsec. The Be filter was removed to measure the laser pulse. X-ray traces measured on targets with 5-μm CH have the same temporal shape as the incident pulse. When the overlayer thickness is reduced from 5 μm to 2 μm, the x-ray signal is more intense and its peak is delayed relative to the laser pulse. The increase in intensity is consistent with that observed in the spectral measurements for 1-keV x-rays. The delayed emission indicates that the ablation layer has reached the Al substrate well after the peak of the laser pulse (but

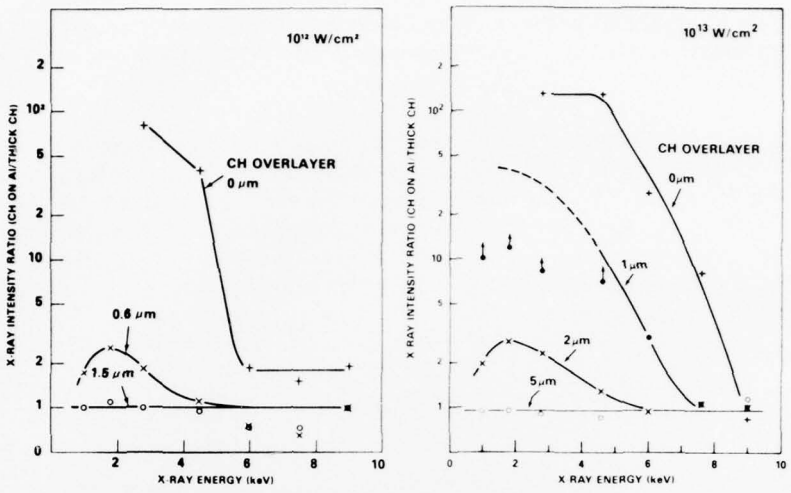

Fig. 15 — X-ray intensity ratios for layered targets at x-ray energies from 1 to 9 keV. Left: Laser irradiance $\simeq 3 \times 10^{12}$ W/cm^2. Right: Laser irradiance $\simeq 1 \times 10^{13}$ W/cm^2. The intensities are normalized to values measured with a 10-μm-thick CH target. The layered targets consist of CH overlayers of different thicknesses on 7-μm-thick Al substrates. The data below 5 keV for a 1-μm-thick CH overlayer at 10^{13} W/cm^2 correspond to lower limits due to saturation of the detector amplifiers.

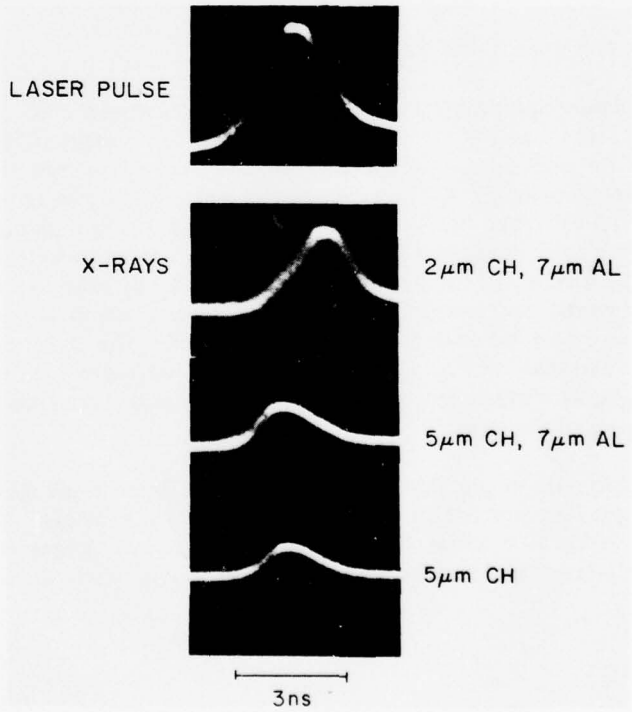

Fig. 16 — A temporal comparison of the emission of 1-2 keV x-rays and the incident laser pulse ($\sim 10^{13}$ W/cm^2) for different layered targets. The horizontal (time) scales are identical for all four traces. The vertical (amplitude) scales are identical for all three x-ray traces.

during the pulse). A similar behavior of increased, but delayed, x-ray emission is observed at 2×10^{12} W/cm^2 when the CH overlayer thickness is reduced from 1.2 μm to 0.6 μm (See Fig. 15b).

Estimates of the ablation depth are made by varying the CH overlayer thickness at irradiances of 10^{13} W/cm^2 and 2×10^{12} W/cm^2. Accordingly, the ablation depth is inferred to be between 2 and 3.5 μm at 10^{13} W/cm^2 and between 0.6 and 1.2 μm at 2×10^{12} W/cm^2, because x-ray emission from the Al substrate was observed to disappear over this range of CH overlayer (See Fig. 15). Ablation depths estimated from these layered target experiments are summarized in Table III and are compared with values determined from particle energy and velocity measurements (to be discussed).

Table III — Summary of Ablation Depth (d) Determinations

Irradiance (W/cm^2)	Layered Target Result	Particle Energy and Velocity Result
1×10^{13}	$2\ \mu m \lesssim d \lesssim 3.5\ \mu m$	$d \approx 3.5\ \mu m$
2×10^{12}	$0.6\ \mu m \lesssim d \lesssim 1.2\ \mu m$	$d \approx 1.3\ \mu m$

D. **Spatially-Resolved X-UV Spectroscopy**:

The x-ray emission spectra presented in Section IIIA suggested that characteristic electron temperatures of ~250 eV and 400 eV are present in the laser-target (CH and Al) interaction region. To search for high temperature emission from the rear-surface of thin targets, a 1-m high-resolution grazing-incidence X-UV spectrograph was employed to record spatially-resolved spectra in the 40-400 eV range on Kodak 101 film. Figure 17a is a photograph of the instrument, which was originally developed for solar spectroscopy from rockets.[35] This spectrograph has been used in the recent past for studies of plasmas heated by ruby, Nd and CO_2 lasers.[36] In the present experiments, the instrument views thin targets which are irradiated at normal incidence with 3-nsec, 15-J Nd laser pulses ($\sim 10^{13}$ W/cm^2). The target plane and the dispersion plane coincide as shown in Fig. 17b. A 500-μm slit inserted between the entrance (spectral) slit and the grating yielded spatial resolution adequate to distinguish radiation from the front and rear surfaces of the target.

Spectra obtained with single shots from 0.5-μm and 7-μm thick Al targets are given in Fig. 17c. The spectra here are similar to those produced by a ruby laser at 10^{12} W/cm^2 and a CO^2 laser at 10^{14} W/cm^2. [36] Lines from transitions in various stages of L-shell ionization appear. The $\Delta n = 1$ (e.g., 2p-3d) lines above 80 eV are strong, while the $\Delta n = 0$ (e.g., 2s-2p)

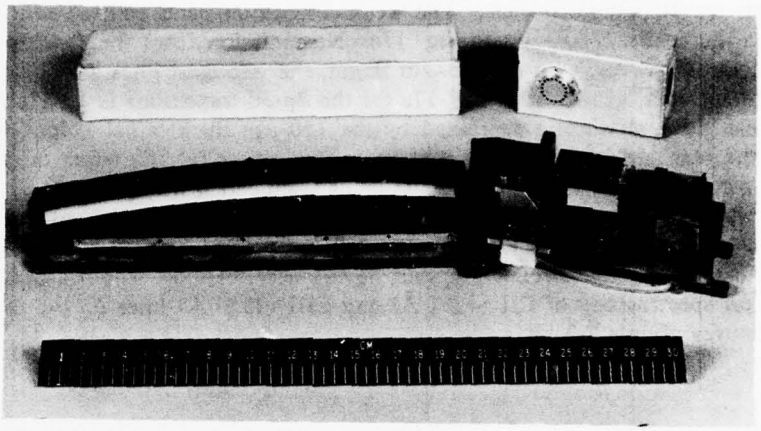

(a)

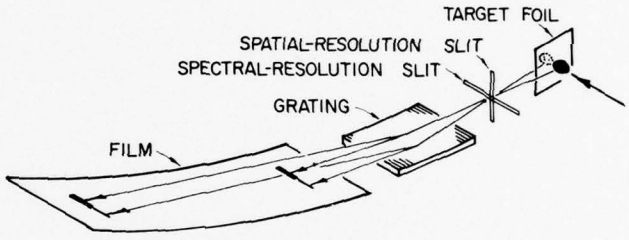

(b)

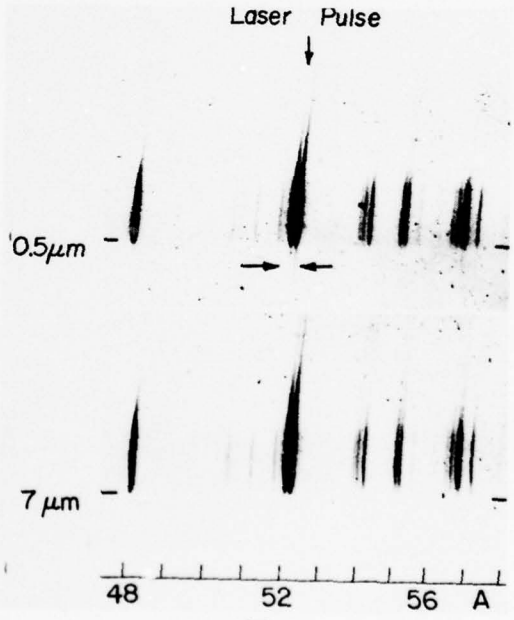

(c)

Fig. 17 — X-UV Spectrograph and typical spectra. (a) Photograph of spectrograph. (b) Schematic of spectrograph and target geometry. (c) Space-resolved spectra obtained at $\sim 1 \times 10^{13}$ W/cm^2 on a 0.5-μm Al target (top) and a 7-μm Al target (bottom). Horizontal marks show the limit of front surface radiation. Radiation from the rear surface of the thin Al target is visible between the arrows.

lines at longer wavelengths are weak. The weak continuum band emitted near the target surface indicates the spatial resolution in Fig. 17c. No emission from the rear side is visible for the 7-μm target. However, with the 0.5-μm target, the strongest lines are observed from both front and rear surfaces, as shown in Fig. 17c for the 2p-3d transitions in Li-like Al. The intensity of the rear side emission is decreased by the 150-μm thick target holder which obscured the view of the rear surface. The results indicate that either (a) the target moves rearward by at least 150 μm, so that front surface emission is visible from the rear side, (b) hot plasma expands rearward, or (c) a combination of these effects. Information about the motion of the foil discussed later in this report suggests that (a) is the correct explanation. In fact, the rear surface of the targets remain relatively cold during acceleration. Time-integrated but space-resolved optical spectroscopy of CII (4267 Å) and CIII (4326 Å) lines on the rear surface suggests temperatures of only 2-3 eV.

V. ABLATIVE ACCELERATION OF LASER-IRRADIATED THIN-FOIL TARGETS

In this section, we study the ablative acceleration of thin foil targets experimentally and compare these results with a simple hydrodynamic model. Ablative acceleration utilizes the thrust of plasma blowoff on the laser side of the target to accelerate the remaining portion of the target to high speed — much as in a rocket. We address such questions as the final target velocities that can be achieved and the fraction of the absorbed laser energy that can be converted into kinetic energy of this accelerated foil. First, we review a simple analytical model which uses basic conservation laws to describe the hydrodynamic behavior of the target. This model uses the analogy to a rocket to provide a relationship between such ablation variables as the hydrodynamic efficiency, the fraction of the mass ablated and the accelerated target-to-ablation velocity ratio. For our experiments, an array of minicalorimeters and time-of-flight charge collectors are used to measure the angular distribution of the ion energy and velocity on both the laser side and the rear side of the target. From these experimental observations, the ablation variables can be deduced and compared with the predicted scalings from the model. Ablative acceleration of foils up to $\sim 10^7$ cm/sec with measured hydrodynamic efficiencies between 2% and 20%, corresponding to the ablation of 5% and 40% of the initial target mass, are shown to be in relatively good agreement with the model.

A. Hydrodynamic Model:

The model considers the 1-D acceleration of a target due to the rocket effect of the laser-driven ablation.[37] This analogy to a rocket is used to describe the hydrodynamic behavior of the target during the acceleration phase. In this case, a rocket of mass M and velocity v is accelerated by the steady-state exhaust of the propellant at a constant velocity u defined in the accelerated rocket frame of reference. At any given time, the rate of change of momentum of the rocket is

$$\frac{d}{dt} Mv = - \frac{dM}{dt} (u - v), \tag{4}$$

or equivalently,

$$M \frac{dv}{dt} = - u \frac{dM}{dt}. \tag{5}$$

Equation (5) is integrated to yield the final mass M and velocity v of the rocket as a function of the propellant velocity u and initial rocket mass, M_o, giving,[37]

$$\frac{v}{u} = ln\left(\frac{M_o}{M}\right). \tag{6}$$

Equation (6) also applies to the case of steady-state laser driven ablation.[38,39] Hydrodynamic calculations and experiments have shown that a steady state ablation, with a well defined ablation velocity u, is set up within the first nanosecond of the interaction.[5] It is to be noted that Eq. (6) does not require any assumptions about laser energy transport or density and temperature profiles.[40] These factors are, in fact, lumped into a knowledge of the ion ablation velocity parameter u which is determined experimentally. For small mass losses, it can also be verified that Eq. (6) reduces to

$$\frac{v}{u} \simeq \frac{\Delta M}{M_o}, \tag{7}$$

where $\Delta M = M_o - M$.

The hydrodynamic conversion efficiency, defined as the final kinetic energy of the target divided by the absorbed laser energy, can also be derived from Eq. (6) and the conservation of energy. The rate of absorbed laser energy $\dot{E}_a$ must be balanced by the energy dissipated in the ablation and acceleration of the target, assuming negligible radiative losses,

$$\dot{E}_a = \frac{d}{dt}\left(\frac{1}{2} Mv^2\right) + \frac{1}{2} (-\dot{M})(u - v)^2. \tag{8}$$

Using Eq. (5), Eq. (8) reduces to

$$\dot{E}_a = -\frac{1}{2} u^2 \frac{dM}{dt}. \tag{9}$$

Equation (9) can now be integrated to give

$$E_a = \frac{1}{2} u^2 (M_o - M), \tag{10}$$

where E_a is the absorbed laser energy. The hydrodynamic conversion efficiency is

$$\eta_h = \frac{1}{2} Mv^2 / E_a. \tag{11}$$

Using Eq. (10) and (6) in (11) we then obtain simply,

$$\eta_h = \frac{(v/u)^2}{\exp (v/u) - 1}, \tag{12}$$

which again reduces for small mass losses to

$$\eta_h \simeq v/u \simeq \frac{\Delta M}{M_o}. \tag{13}$$

The ablation pressure (or thrust) exerted on the target by ablation is also a useful parameter that can be derived from the model. From the fluid equations, one can derive a relation for the pressure at peak density (the ablation surface) expressed by,

$$P_a = m\frac{dv}{dt} = -u\frac{dm}{dt} \tag{14}$$

where m is the mass per unit area. A relation useful for the experimental determination of P_a is given by

$$P_a = \rho X_o \frac{v}{\tau_e}, \tag{15}$$

where ρ and X_o are respectively the target material density and initial foil thickness, and τ_e is the laser pulse duration. For a one-dimensional ablation, the ablation pressure can also be related to the absorbed laser flux I_a and the ablation velocity by using Eq. (9),

$$P_a = \frac{2I_a}{u}, \tag{16}$$

the same relation used in Eq. (2).

Equations (6) and (12), relating the ablation variables, are plotted in Fig. 18. As expected, when the target velocity becomes comparable to the ablation velocity, the hydrodynamic efficiency increases up to a maximum of 65% (where 80% of the initial mass is ablated). It should be noted here that the material ablated with $u/v < 1$ is actually moving in the direction of the accelerated target. To avoid experimental difficulties associated with large mass losses and $u/v < 1$, the data presented below are obtained for cases where Eq. (13) applies, i.e., $u/v >> 1$.

B. Ablation, Acceleration and Efficiency Measurements:

Experimentally, several diagnostics are used to measure ablation observables. In this section, we mostly discuss asymptotic (late time) measurements of the ablation and the accelerated target parameters. Figure 19 shows the typical case of a slug of material accelerated from a 15-μm thick CH foil due to ablation. The angular distribution of the ion blowoff on the laser side is measured with minicalorimeters for the ion energy, and time-of-flight charge collectors for the ion velocities. The same thing is done on the rear of the target for the accelerated target material. Typical charge collector traces are shown in Fig. 19 for the front and rear of the target. Assuming a constant charge state and secondary electron coefficient over the time history of the collector trace, an average velocity is inferred from the velocity distribution unfolded from each charge collector signal. These are reasonable assumptions for the ablation peak because it is relatively narrow in energy spread and uncomplicated in temporal shape. From the angular distributions of energy and velocity one can obtain the average ion ablation velocity u over all angles on the laser side. Similarly one also obtains the final target velocity v from the angular distribution of the accelerated target material. The hydrodynamic efficiency is obtained directly from the integration of the angular energy distributions on the rear side. Finally, the fraction of the mass ablated is inferred from the proper angular integration of the energy divided by the square of the velocity on the laser side. The measured ablation variables u, v, η_h and $\Delta M/M_o$ are shown in Fig. 19 for the case of a 15-μm CH foil irradiated at 1×10^{13} W/cm^2 for 3 nsec. The ablation velocity and the final target velocity were also cross-checked experimentally with optical diagnostics discussed in the following section.

By varying the initial foil thickness it is possible to control the fraction of the mass ablated and obtain different values for the hydrodynamic efficiencies and the final target velocities. For relatively small mass losses the ablation velocity shown in Fig. 19 remains the same for different foil thickness. The experimental results on ablative acceleration of thin foil targets are shown in Fig. 20 together with a comparison of the scaling between the ablation variables obtained from the rocket model.

The dashed line in Fig. 20 results from a correction introduced into the 1-D model to account for the fact that the ablation ions are not all blowing-off at normal incidence from the target but have an experimentally observed average cone angle of 40° with respect to the target normal.[41] This correction has the effect of lowering the theoretical hydrodynamic efficiency predicted for a 1-D ablation in planar geometry. It is assumed here that only the velocity component normal to the target surface can contribute to the transfer of momentum to the accelerated foil. Accordingly, the normal components of the observed ablation and target velocities are used in the data points in Fig. 20. The normal components of the ablation velocities

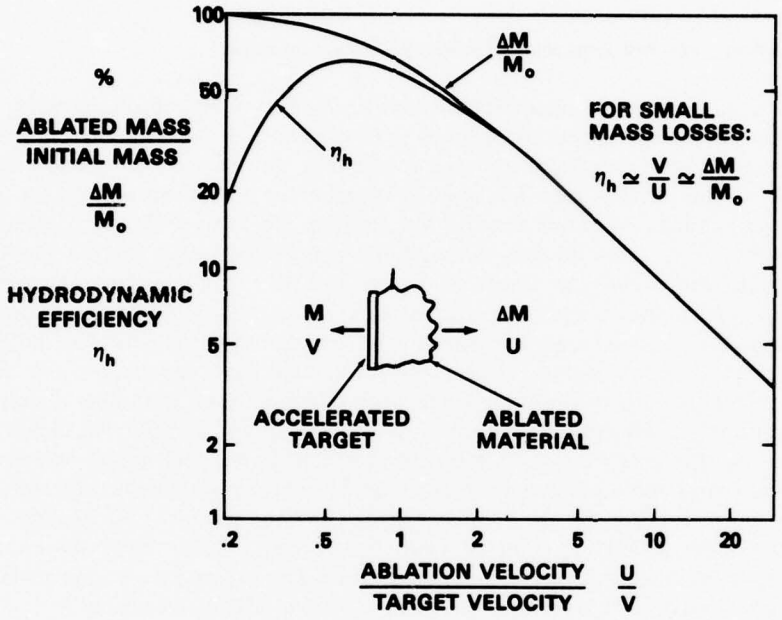

Fig. 18 — Relationships between ablation variables of the acceleration model. The constant ablation velocity u is defined in the moving target frame.

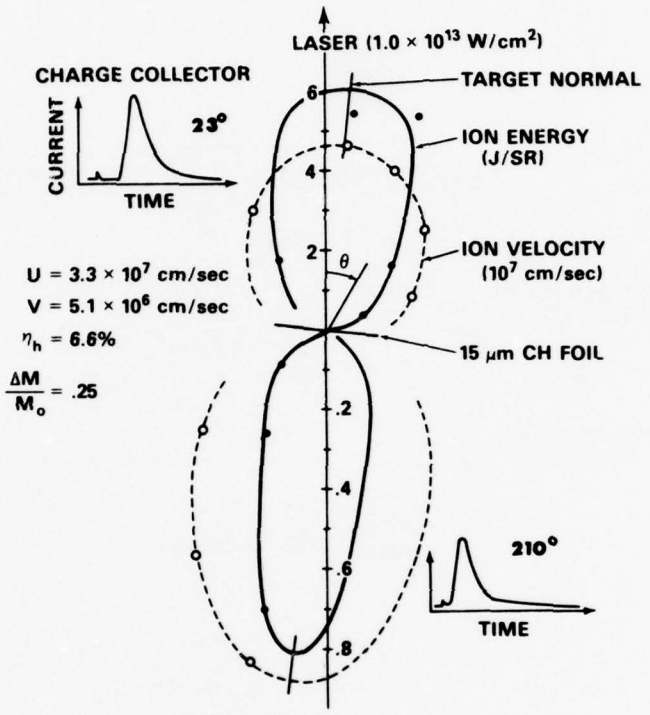

Fig. 19 — Measurement of ablation variables. The average ion ablation velocity u, the final target velocity v, the hydrodynamic efficiency η_h and the mass fraction ablated $\Delta M/M_o$ are inferred from the angular distributions of energies and velocities. Note the expanded scales for quantities measured on the rear surface.

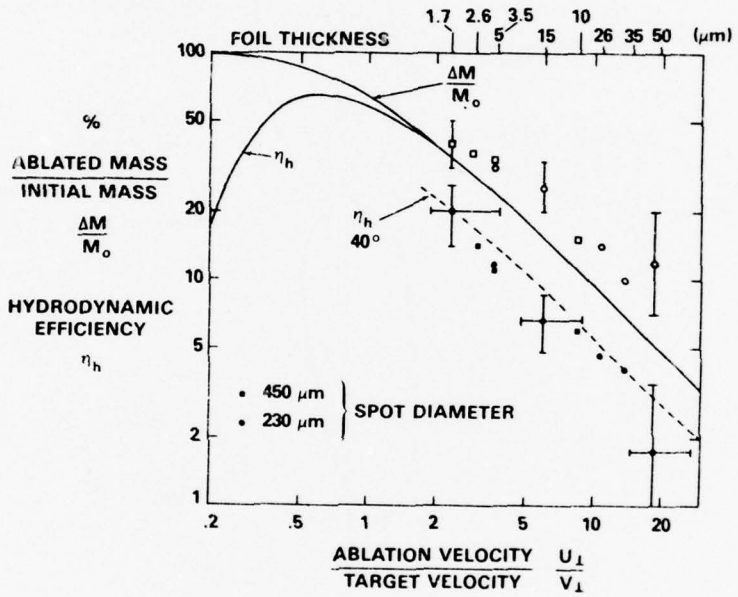

Fig. 20 — Ablative acceleration — comparison of experiment and model. Black and open data points correspond respectively to the hydrodynamic efficiency and ablated mass fraction. Experiments were done by varying foil thickness and spot diameter. The dashed line is the 2-D correction to the 1-D model. The error bars are the greater of standard deviation and estimated measurement uncertainty.

at 40° are, respectively, 2.5×10^7 and 1.9×10^7 cm/sec for the 230-μm (1×10^{13} W/cm^2) and 450-μm (3×10^{12} W/cm^2) laser spot sizes. The latter is consistent with a previous experiment.[41] The effective cone angle of emission of the accelerated target material is approximately 35° (half the mass within 35°) with respect to the target normal.

Figure 20 shows that the measured hydrodynamic efficiencies when plotted against the ablation-to-target velocity ratios are in good agreement with the scalings from the model. The fraction of the mass ablated appears to be systematically too large but is still in reasonable agreement. Ablation depths inferred from layered target experiments (described in Section IV C and Table III) are also in good agreement with these measurements. It is not clear at this point whether the source of error in the fraction of the mass ablated is due to overestimating the ablated mass or underestimating the accelerated mass. However, it should be pointed out that a substantial fraction of the mass, moving at a very low velocity, due to edge effects or a finite laser pulse width, could escape detection because of inherent characteristics of the diagnostics used in these experiments. There is some indication that this effect has been observed using the ballistic pendulum momentum detectors. Nonetheless, as shown in Fig. 20, we have obtained hydrodynamic efficiencies as high as 20%, while ablating 40% of the mass, with an ablation-to-target velocity ratio of 2.3. These results are in good agreement with the scaling obtained from the model between the ablation variables when 2-D effects are taken into account.

The ablation pressure can also be inferred from Eq. (15). For thick targets and our 3 nsec laser pulse, the ablation pressures are 1 and 3 Mbar for the 450-μm (3×10^{12} W/cm^2) and 230 μm (1×10^{13} W/cm^2) laser spot sizes respectively.

C. **Edge Effects**:

One of the experimental difficulties that appeared during these experiments involves edge effects associated with the use of wide, thin foil targets with a finite laser spot size. This effect is illustrated schematically in Fig. 21. For large target velocities, the displacement of the accelerated foil becomes comparable to the diameter of the ablated region, so that edge effects can be important. The net effect is that the absorbed laser energy (heat) is not only transported from the absorption region to the ablation layer of the accelerated target, but also to the edge of the initial foil. The effective diameter of the ablated material is therefore increased beyond the laser spot size with, accordingly, a decrease in the penetration depth of the thermal wave into the material. Quantitative edge effect results are shown in Fig. 22 for the two laser spot sizes in use in the ablation experiments. The ablated diameter is inferred from the experimental ablation velocity u, the ablated thickness and conservation of energy. In Fig. 22, we see that the penetration depth of the thermal wave into the material decreases with foil thickness with a corresponding increase in the effective ablation diameter. For both laser spot sizes, a regime is reached where the ablated thickness of material decreases with the foil thickness. However, as expected, the fractional increase of the ablated diameter for a given fraction of the mass ablated is reduced for the larger spot size. These results indicate that larger laser spot sizes or, possibly, finite diameter targets are required to limit edge effects for larger target velocities. It should be emphasized, however, that the scaling between the ablation variables is still valid even when the ablated thickness of material is dependent on foil thickness.

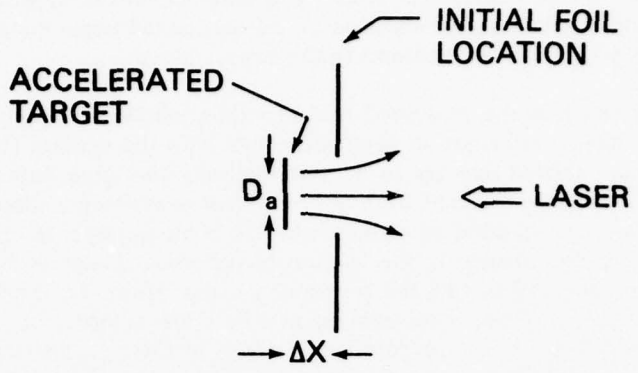

Fig. 21 — Accelerated foil geometry, showing where edge effects are important for $\Delta x \approx D_a$.

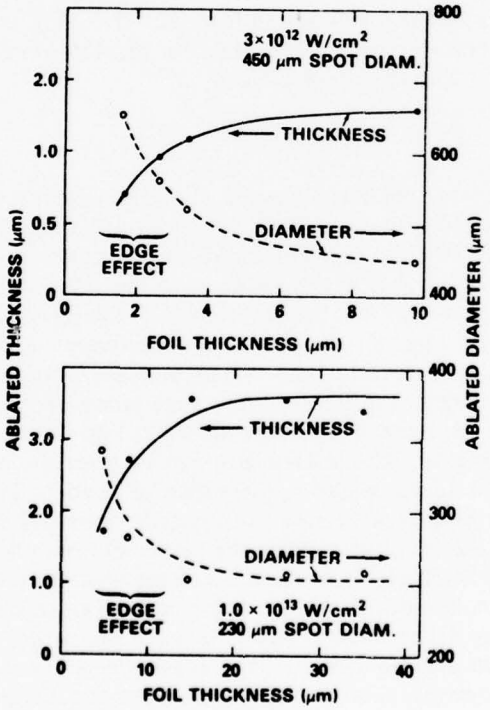

Fig. 22 — Edge effects, experimental. Ablated thickness and effective ablated diameters versus foil thickness for two conditions of irradiance and spot diameters.

D. **Summary**:

It is shown in this section that at Nd-laser irradiances of 3×10^{12} and 10^{13} W/cm^2, ablation velocities are ideal for efficient acceleration of foils up to speeds of $\sim 2 - 3 \times 10^7$ cm/sec as anticipated in some pellet designs.[2,18]

Foils are, in fact, ablatively accelerated to a velocity, so far, of $\sim 10^7$ cm/sec with a hydrodynamic efficiency of $\sim$20% in good agreement with a simple model. Overall, because the absorption fraction is >80%, more than 16% of the incident laser energy ends up as kinetic energy in the accelerated foil. The crucial question of the stability of the accelerated foil will be addressed in future experiments.

In the next section we provide evidence that the target is *ablatively* accelerated rather than exploding or being spalled. Also, details of the rear and front surface motions are obtained in several unique ways.

VI. FRONT AND REAR SURFACE BEHAVIOR

In this section we use optical diagnostics to take a much closer look at the behavior of both the front surface (laser side) and the rear surface (accelerated side).

The front surface motion is interesting from several points of view. Hydrodynamic codes, used to compare with these sets of experiments, calculate front surface behavior most easily. Thus, the experiment can be used to set up initial conditions for the code, and/or the code-determined front surface motion can be compared directly with experiment to ensure proper treatment of the interaction physics.

The rear surface is studied carefully because: 1. We want to be confident that the foil is ablatively accelerated and is not in an exploding pusher or spall regime. 2. Measurement of the target velocity by several means adds confidence to the ablation and efficiency determinations. Additional information about the state-of-matter and structure of the rear surface are also obtained in some methods. 3. Finally, optical diagnostics give 2-D information on beam uniformity requirements and hydrodynamic stability of the rear surface.

The front surface motion is examined with short-pulse interferometry and shadowgraphy which follows the plasma development from its initial formation. The rear surface motion is optically studied using the short-pulse interferometry and shadowgraphy, Doppler sounding, long-pulse streak shadowgraphy and time-integrated spectroscopy.

A. Front Surface Plasma Development:

Figure 23 shows a schematic diagram of the interferometer arrangement. The 400 psec, 5320-Å probe beam as described earlier (Section II C), is optically delayed to allow variation of the relative timing between the probe pulse and the main laser pulse. The probe beam is then directed through the plasma in the target chamber parallel to the target surface, giving an edge-on view. Probe beam light leaving the plasma region passes through two lenses (f/6) which serve both to maintain the collimated beam for the interferometry and also to magnify the image on the recording film. The interferometer is a modified Jamin interferometer used in a mode described by H. Azechi, et al.[42] The advantage of this type of interferometer is that it can be placed some distance from the target chamber, where it does not block other diagnostic devices and can be easily adjusted. The interference pattern is recorded on Polaroid film after passing through an interference filter and attenuating filters. Also, simultaneous shadowgrams are taken by splitting off the image in front of the interferometer.

The plasma can be monitored in time on both sides of a thin foil target using this interferometer with the short duration probe pulse. This allows a determination of the initial time for the plasma to be produced, and also, if the time-resolution is sufficient that the fringes are frozen, allows the electron density to be determined. This has been done for a 7 μm thick aluminum foil target using a laser pulse of about 16 J and 3 nsec duration and a target irradiance of $\sim 3 \times 10^{13}$ W/cm^2. Representative interferograms taken very early in time, Fig. 24, shows that plasma formation occurs approximately 8 nsec before the peak of the heating pulse.

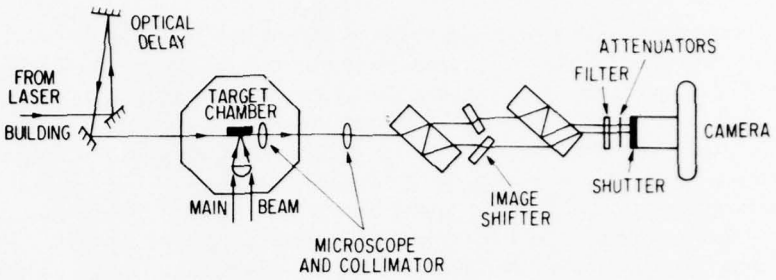

Fig. 23 — Experimental arrangement and modified Jamin interferometer.

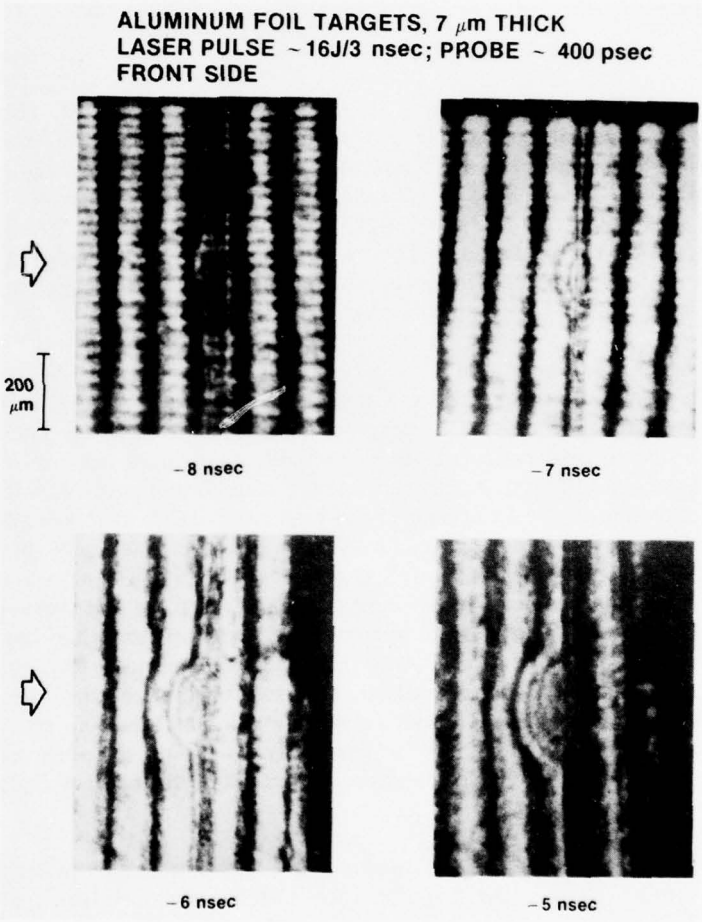

Fig. 24 — Front surface interferograms. Times noted are with respect to the peak of the incident laser pulse. Laser is incident from the left.

For a heating pulse with a temporal shape as shown in Fig. 4, the distance that the electron density contour of $\sim 10^{18}$ cm^{-3} has propagated on the laser side of the foil is shown in Fig. 25. Here again it is noted that a detectable plasma can be seen as early as 8 nsec prior to the peak of the main laser pulse. This initial plasma moves at a constant velocity of 6.7×10^6 cm/sec until -2 nsec, and then speeds up to 3.5×10^7 cm/sec through the time of the peak of the incident laser pulse. By comparing the pulse shape in Fig. 4 to Fig. 25, it is seen that the first measurable plasma is produced at a power density of $\sim 3 \times 10^9$ W/cm^2 and grows approximately linearly until a power density of 20% of peak power is reached (6×10^{12} W/cm^2). From this power density to peak power, the faster velocity is maintained. The later plasma velocity is approximately the same as the plasma velocity measured with time-of-flight ion probes, namely 3.3×10^7 cm/sec (Fig. 19).

B. **Rear Surface Motion**:

1. Interferometry and Shadowgraphy Methods.

The interferometer can also be used to observe the motion of the rear surface of the accelerating foil. An interesting example of this is the rear surface interferograms of 16 μm thick CH foils shown in Fig. 26. One notes the early and somewhat irregular plasma at +1 nsec, followed by a neat plasma slug at +2 nsec, and then a more divergent plasma at +4 and +6 nsec. Also, it is noted that the probe light does not penetrate the dense plasmas at later times on the back side of the target. (This is also the case when shadowgrams are taken.) There is also time-smearing of the fringes due to the duration ($\sim$ 400 ps) of the probe pulse so that fast moving high density regions of the plasma are not resolved.

Figure 27 shows shadowgrams of 15-μm CH foils irradiated at 10^{13} W/cm^2. This figure is a composite taken from a number of shots. Times with respect to the peak of the heating pulse are indicated to the left, starting at -1 nsec and continuing to +11 nsec. The dark regions on the front side are due to light refracted out of the collection optics because of the very steep electron density gradient. We know, from ultraviolet and visible spectroscopic measurements, that the emitted material on the front side of the target consists of highly-ionized plasma (C^{+6} and C^{+5}). However, on the colder back side of the target, the dark region may be due to the absorption of light by ejected material as well as refraction at a steep density gradient. Also the backside plasma has a much lower stage of ionization than the front side plasma. Note that the dark region on the rear side of the target appears much later in time than the dark region on the front and that it continues to expand away from the target up to +11 nsec, when it begins to become stringy and diffuse. A plot of distance versus time for the dark region on the back side of the foil is shown in Fig. 28. Early in time one can clearly see an ablative acceleration region, which has a velocity of about 3×10^6 cm/sec followed later by a higher velocity of $\sim 5 \times 10^6$ cm/sec and then an apparent deceleration (which is due to the dark region getting more diffuse).

Figure 29 shows the diameter of the opaque ejecta versus time on the back side of the foil for two foil thicknesses. It is noted that the 5-μm CH foil starts with a smaller diameter of ejecta than the 15-μm foil; however, it increases quickly with time to a much larger diameter. This agrees with the edge effect model presented in Section V C.

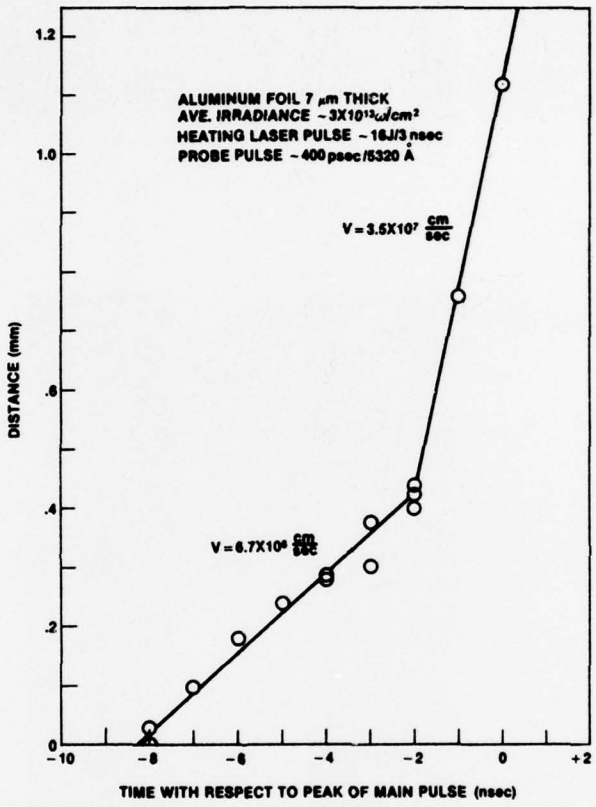

Fig. 25 — Motion of the front surface. Distance versus time of the 10^{18} cm^{-3} density surface.

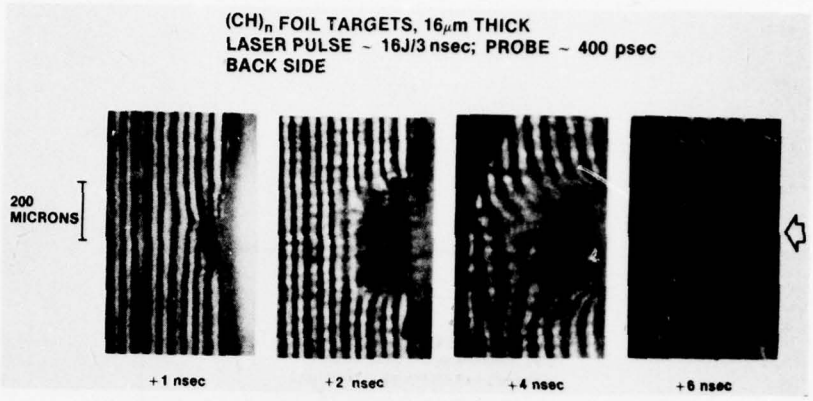

Fig. 26 — Rear surface interferograms. Laser is incident from the right.

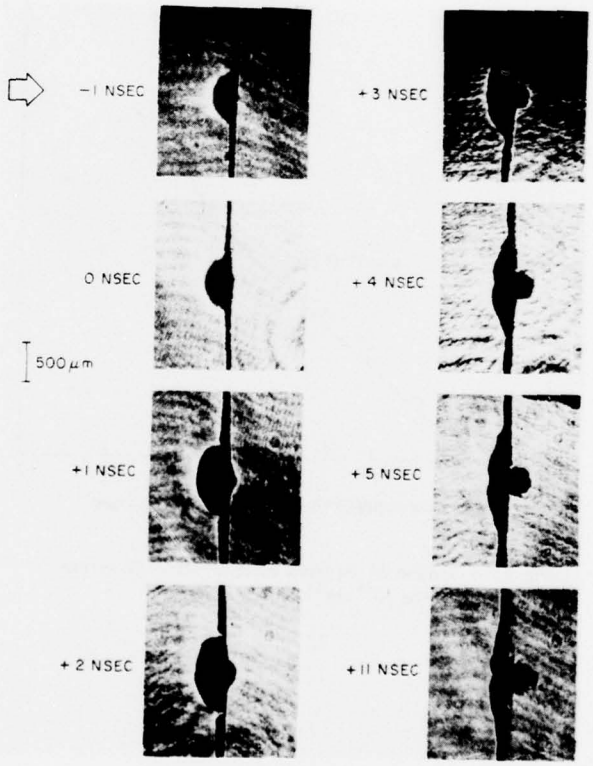

Fig. 27 — Shadowgrams of irradiated 15-μm CH foils at selected times with respect to the peak of the laser pulse. Laser beam is incident from the left.

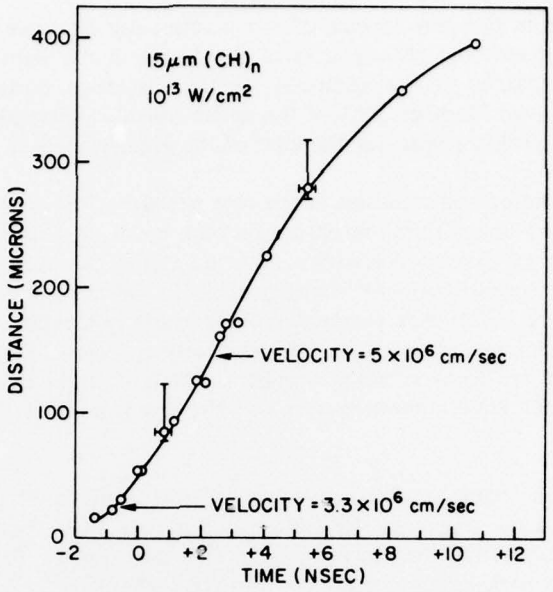

Fig. 28 — Motion of rear surface. Acceleration phase is seen between -1 nsec and +2 nsec. Non-symmetric error bars are due to slight curvature in foil targets.

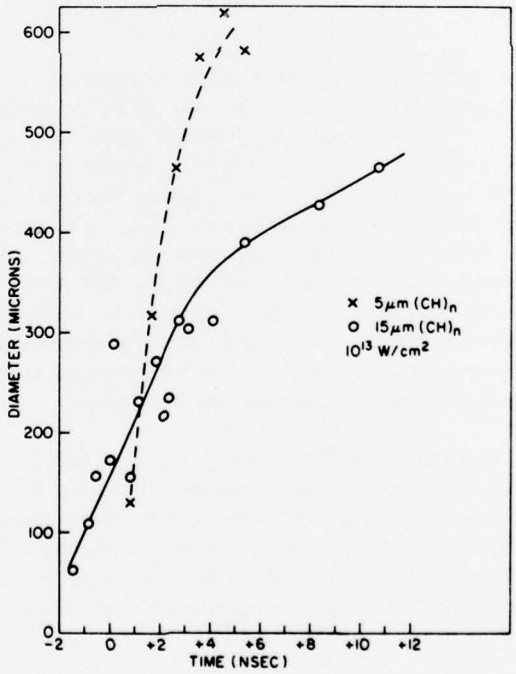

Fig. 29 — Diameter (FWHM) of opaque ejecta from rear of foils of different thicknesses versus time. Edge effect is suggested by larger diameter of thinner foil at late times.

2. Reflected Light Methods.

Scattering light from the rear surface of our accelerating foils can yield several pieces of information. First, conventional photography of the target in the light of the scattered short probe pulse shows snapshots of the geometry of the disturbed portion of the target rear. Second, a spatially-resolved Doppler shift of the probe pulse wavelength scattered off the rear surface gives a velocity profile across the diameter of the accelerated foil.

We conduct the photographic studies of the rear surface of the accelerated thin foil targets by reflecting the subnanosecond duration optical probing beam, described in Section II C, from the target surface. The experimental set-up is depicted in Fig. 30. The 1.06-μm, 3-nsec duration main laser pulse is focused with an intensity of $\sim 10^{13}$ W/cm^2 onto 7 μm thick aluminum foil targets. The 5320-Å, ~400-psec duration probing beam is incident on the rear target surface at near normal incidence. The probe light, diffusely reflected off the dull rear surface of the Al targets, is monitored using cameras at approximately 0° and 45° with respect to the target normal. A 3/4-meter grating spectrograph also allowed Doppler shift measurements to be made.

Figure 31 shows photographs of the reflected light taken by the 0° camera employing f/12 collection optics. The light region is the illuminated target area. No visible disturbance is noted until approximately 1 nsec before the peak of the laser pulse. Shortly after the peak of the main laser pulse, a dark circular region is observed where the reflected light intensity is reduced by at least 6 dB over that of the adjacent, apparently undisturbed, aluminum surface. Similar results from the 45° camera suggests that absorption of the probe light, in addition to any light scattering processes, may be causing this darkened region. Near the peak of the main laser pulse, the darkened region has dimensions about 30% larger than that of the incident focal spot.

As noted earlier, a spectrograph is employed to measure any Doppler shifts in the reflected probe light. The spectrograph is stigmatic and, thus, by focusing the image of the target onto the entrance slit of the spectrograph, Doppler shifts (and thus velocities) could be measured as a function of position across the interaction region on the target. Figure 32 shows the results of Doppler shift measurements at time -0.8 ns (before) the peak of the main laser pulse and +0.2 ns (after) the peak of the main laser pulse. For these results a 7-μm Al foil target is again employed. Note that at the earlier time the velocity distribution has a 320-μm spatial FWHM which is larger than the laser spot size ($\sim$ 230 μm). At the later time, however, a slug of material with dimensions similar to that of the main laser spot size has broken away from the rest of the target and is accelerated to a nearly spatially uniform velocity of $\sim 10^6$ cm/sec. Doppler shift measurements attempted at still later times are hampered by the appearance of the dark region in the target image mentioned previously.

At t = +0.2 nsec, approximately 40% of the total laser energy has been incident on the target. (The laser pulse is assymetric in time) A simple calculation employing the measured ion blowoff velocities, conservation of energy and momentum, and assuming the area of the target accelerated to be the same as the laser spot size, predicts a velocity of 1.6×10^6 cm/sec at t = +0.2 nsec, and a final velocity of 4×10^6 cm/sec for the experimental conditions of Fig. 32. The (relatively small) discrepancy between the velocity obtained through this simple calculation

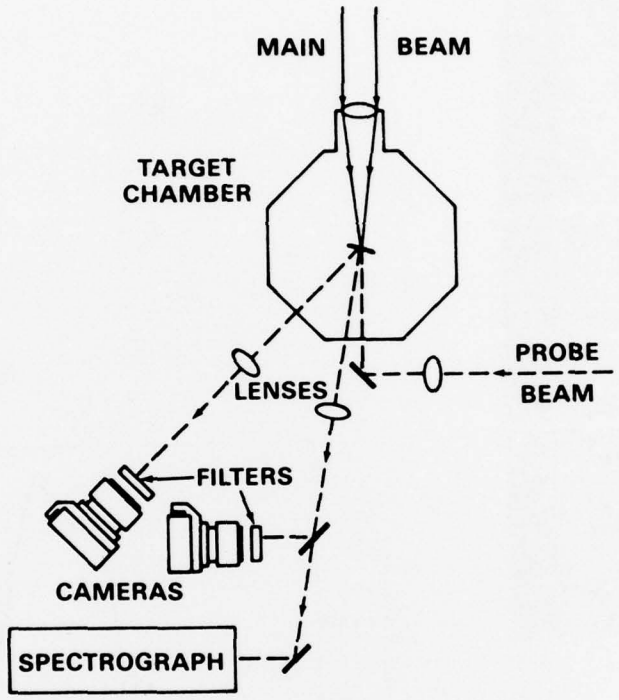

Fig. 30 — Reflected probe light arrangement.

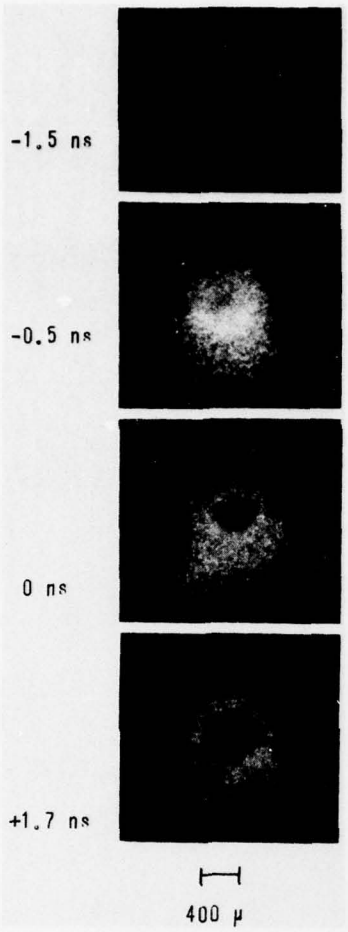

Fig. 31 — Photographs of rear surface in probe light at indicated times.

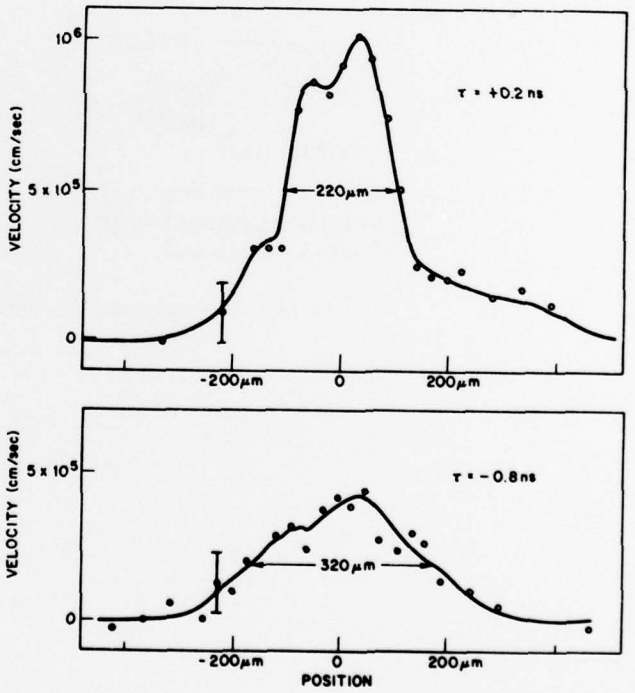

Fig. 32 — Doppler shift velocity determinations across the rear surface of 7-μm Al target at two times. Laser irradiance is 1×10^{13} W/cm^2 with a focal diameter of 230 μm.

and the experimental results can be the result of momentum transferred to the target outside the laser focal distribution, i.e., an edge effect. At the relatively low accelerations involved early in the laser pulse, the shear strength of the foil target may, for a time, allow the irradiated target to drag along a part of the non-irradiated target. Later in the pulse this may not be a significant effect.

3. Streak Shadowgraphy Method

All the methods described so far to monitor the motion of the rear surface of the accelerating foil were either time-integrated or sampled at discrete times. Streak photography, on the other hand, provides a continuous temporal measurement of the rear surface position. Here one can "see" the continuous acceleration of the foil due to ablative acceleration, and ensure that rear surface ejecta is not dominating the dynamics or diagnostics. Spallation or shock wave phenomena on the rear surface would probably be characterized by a *more rapid* change in velocity than that of ablatively driven motion.

We will see that the streak camera photographs of the rear surface motion, taken in our experiments, agree with the ablatively driven model and with all the discrete and time-integrated measurements previously discussed.

The experimental arrangement is very similar to that used for interferometry and shadowgraphy, shown in Fig. 23, except for two major features. First, the interferometer is eliminated and the streak camera replaces the still camera. The streak camera (EPL, $\tau_r \approx 5$ psec, S-1 photo cathode) is arranged with its slit imaged normal to the target surface, as indicated on the top of Fig. 33. Second, the backlighting source is still the 5320-Å probe beam, but, for the purposes of streak photography, its duration is left at $\sim$2 nsec and not temporally shortened as in the other optical diagnostic cases. Both the streak camera timing and backlighting source are delayed together to obtain a string of successive 2-nsec segments such as shown in Fig. 33.

A smooth and continuous acceleration of the rear surface is seen from t = -1 nsec until about +2 nsec indicating ablative acceleration. These data are reproducible from shot-to-shot with only one or two exceptional shots. A plot of velocity versus time, averaged over many shots is shown in Fig. 34 for incident irradiance of 1×10^{13} W/cm^2. (Error bars denote an uncertainty in the velocity measurements of around 20% and not a variation in the shape of the curve.) From the slope of the velocity versus time curve near the peak of the laser pulse we infer a peak acceleration of $8 \pm 2.4 \times 10^{14}$ cm/sec^2 for this shot. Also shown in the same figure are data from the shadowgraphy (Figure 28 of Section VI B), and from the time-of-flight and calorimetry measurements (Figure 19 of Section V B), all in relatively good agreement. Doppler shift velocity determinations are made, so far, only with Al targets and could not be put on this diagram. However, they too agree with the other methods of obtaining velocity.

The fact that we are able to measure the dynamics of the target foil rear surface by several independent methods, with results that are self-consistent, that demonstrate a continuous acceleration, gives us good confidence that we are indeed studying ablatively driven foil acceleration.

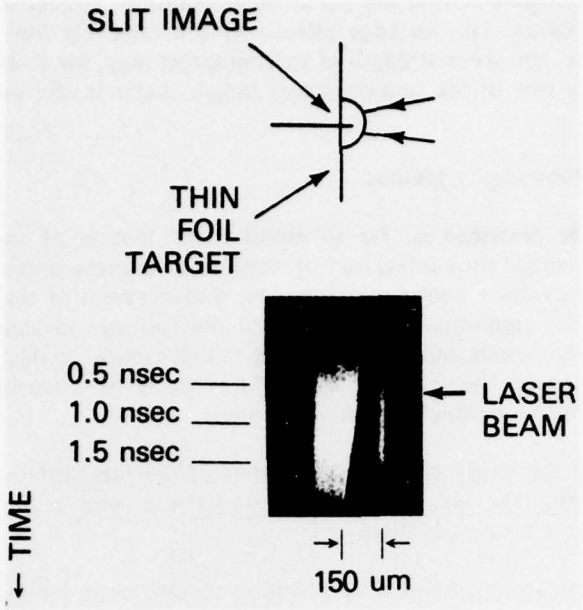

Fig. 33 — Streak shadowgrams of rear surface motion. Top: Geometry of streak camera slit image across foil edge. Bottom: A streak photo showing distance-versus-time development of rear surface of a 15-μm thick CH foil at irradiance 1×10^{13} W/cm^2. Bright region on the front surface (right) is second-harmonic emission from the laser interaction region.

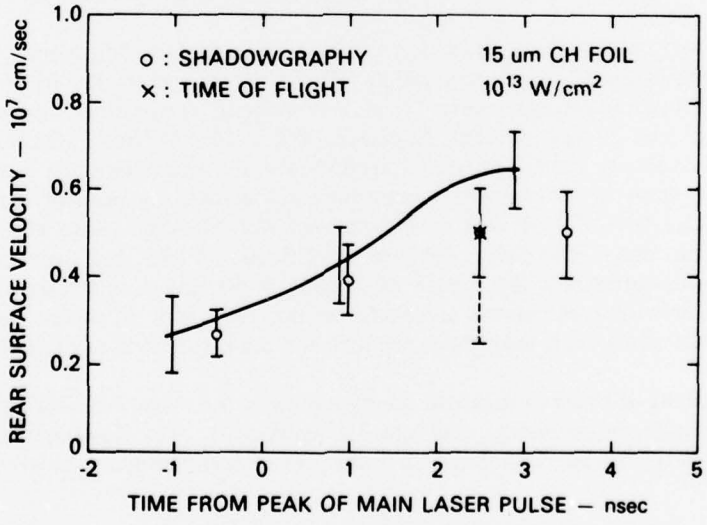

Fig. 34 — Rear surface velocity versus time obtained with streak camera data (solid curve), shadowgram frames (open circles) and asymptotic charge collector time-of-flight point (*).

VII. SUMMARY AND CONCLUSIONS

The theme of this report has been a discussion of measurements of the laser-plasma interaction in the $10^{12}-10^{14}$ W/cm^2, multi-nanosecond regime. We have kept an eye towards the laser fusion application, i.e., the efficient and stable acceleration of a pellet surface. Figure 35, schematically shows the relationship between the ablation pressure and hydrodynamic efficiency for a particular wavelength of laser irradiation. As one decreases the pressure (i.e., decreases the laser irradiance I_L, a la Eq. 17), the efficiency increases. However, at some point hydrodynamic stability of the accelerated shell (or foil) will put a lower limit (dashed line) on the pressure, because the aspect ratio of the shell, $R/\Delta R$, is inversely proportional P. We are attempting to find that optimal point for Nd-laser irradiated targets which maximizes efficiency with sufficient stability.

We have shown here, in the regime of 10^{12} W/cm^2 to 7×10^{14} W/cm^2, 3-nsec Nd-laser pulses, that the absorption is good ($>50\%$) and that thin foils can be ablatively accelerated up to $\sim 10^7$ cm/sec with good ($\sim 20\%$) efficiency. These results are in reasonable agreement with a simple hydrodynamic model. We have also addressed details of the thermal conductivity both axially (related to ablative depth and thermal heat velocity) and laterally (related to beam uniformity requirements). These results are encouraging for the laser fusion application. A one-dimensional Lagrangian hydrodynamic code with classical transport coefficients has been run at NRL for these experimental conditions.[43] Code and experimental results for ablated mass fractions, hydrodynamic efficiencies, ablation and target velocities, etc., compare quite closely. Future experiments will deal more fully with beam uniformity requirements and the stability of the accelerating foils.

ACKNOWLEDGMENTS

The authors appreciate the valuable aid towards the work reported here given by: J. Boris, P. Moffa, M. Fink, N. Nocerino, E. Turbyfill, R. McGill and T. Derieux. This work is supported by the U.S. Department of Energy.

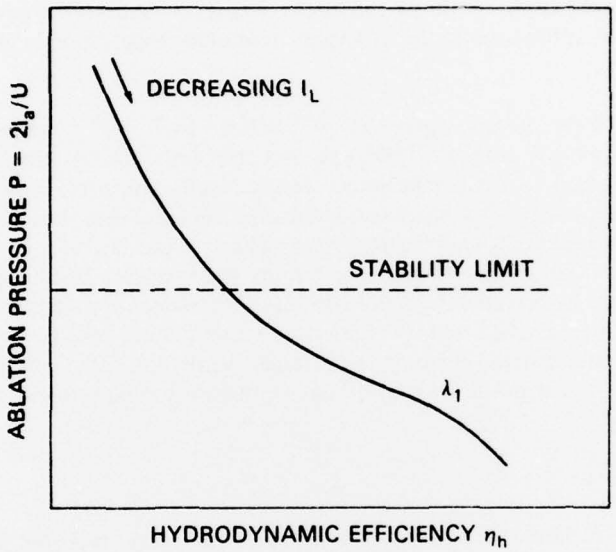

Fig. 35 — Schematic diagram suggesting a direct relationship between hydrodynamic efficiency and ablation pressure, for a given laser wavelength. Hydrodynamic stability puts a lower limit on acceptable ablation pressure.

REFERENCES

1. B. H. Ripin, et al., Bull. Am. Phys. Soc. **23**, 786 (1978); R. R. Whitlock, et al., ibid.; R. Decoste, et al., ibid; S. P. Obenschain, et al., ibid.; E. A. McLean, et al., ibid; C. M. Armstrong, et al., ibid.

2. J. H. Nuckolls et al., European Conf. on Laser Int. with Matter, Oxford, England, Sept. 1977.

3. O. N. Krokhin, Y. A. Mikhailov, V. V. Pustovalov, A. A. Rupasov, V. P. Silin, G. V. Sklizkov and A. S. Shikanov, Sov. Phys. JETP **42**, 107 (1976).

4. N. G. Kovalskij, M. T. Pergament and P. P. Pashinin, presented at IAEA Meeting, San Francisco, CA, Jan. 1978.

5. J. P. Anthes, M. A. Gusinow and M. K. Matzen, Phys. Rev. Lett. **41**, 1300 (1978); M. A. Gusinow, J. P. Anthes, M. K. Matzen, and D. Woodall, Appl. Phys. Lett. **33**, 800 (1978); M. K. Matzen and R. L. Morse, Bull. Am. Phys. Soc. **23**, 787 (1978).

6. S. Zwiegenbaun, Y. Gazit and Y. Komet, Plasma Phys. **19**, 1035 (1977).

7. B. Arad, S. Eliezer, Y. Gazit, H. M. Loebenstein, A. Zigler, H. Zmora and S. Zweigenbaum, to be puslished.

8. J. H. Nuckolls, L. Wood, A. Thiessen and G. Zimmerman, Nature (London) **239**, 139 (1972).

9. B. H. Ripin, NRL Memo Report No. 3684, 1977.

10. B. H. Ripin, F. C. Young, J. A. Stamper, C. M. Armstrong, R. Decoste, E. A. McLean and S. E.Bodner, Phys. Rev. Lett. **39**, 611 (1977).

11. R. C. Malone, R. L. McCrory and R. L. Morse, Phys. Rev. Lett. **34**, 721 (1975).

12. B. H. Ripin, P. G. Burkhalter, F. C. Young, J. M. McMahon, D. G. Colombant, S. E. Bodner, R. R. Whitlock, D. J. Nagel, D. J. Johnson, N. K. Winsor, C. M. Dozier, R. D. Bleach, J. A. Stamper, and E. A. McLean, Phys. Rev. Lett. **34**, 1313 (1975).

13. W. M. Manheimer, D. G. Colombant, and B. H. Ripin, Phys. Rev. Lett. **38**, 1135 (1977); W. M. Manheimer and D. E. Colombant, Phys. Fluids **21**, 1818 (1978).

14. R. Decoste and B. H. Ripin, Phys. Rev. Lett. **40**, 34 (1978); R. Decoste, NRL Memo Report No. 3774 (1978).

15. J. A. Stamper and B. H. Ripin, Phys. Rev. Lett. **34**, 138 (1975); J. A. Stamper, E. A. McLean and B. H. Ripin, Phys. Rev. Lett. **40**, 1177 (1978).

16. A. Raven, O. Willi and P. T. Rumsby, Phys. Rev. Lett. **41**, 554 (1978).

17. B. Arad and S. Eliezer, Appl. Phys. Lett. **32**, 401 (1978).

18. D. Henderson, private communication, (1977); Y.F. Afanas'ev, N.G. Basov, E. Gamalii, O.N. Krokhin and V.B. Rozanov, JETP Lett. **23**, 556 (1976).

19. G. Taylor, Proc. Roy. Soc. **201A**, 192 (1950).

20. K. A. Brueckner and S. Jorna, Rev. Mod. Phys. **46**, 325 (1974).

21. J. P. Boris, Comm. On Plasma Phys. and Cont. Fusion **3**, 1 (1977).

22. F. C. Young, R. R. Whitlock, R. Decoste, B. H. Ripin, D. J. Nagel, J. A. Stamper, J. M. McMahon and S. E. Bodner, Appl. Phys. Lett. **30**, 45 (1977); B. Yaakobi and T. C. Bristow, Phys. Rev. Lett. **38**, 350 (1977).

23. Y. B. Zel'dovich and Y. P. Raizer, "Physics of Shock Waves and High-Temperature Hydrodynamic Phenomena," Academic Press, NY (1966).

24. B. H. Ripin, in NRL Memo Report No. 3315 pg. 20, (1976) (ed. S. E. Bodner).

25. J. M. McMahon in NRL Memo Report No. 3591, (1977) (ed. S. Bodner).

26. S. R. Gunn, Lawrence Livermore Lab. Report UCID-17308 (1976).

27. A. Williams, in 1975-LASL Annual Report No. LA-6050-PR, 82 (1976) (ed. F. Skoborne).

28. B. H. Ripin, Appl. Phys. Lett. **30**, 134 (1977).

29. J. P. Anthes, M. A. Palmer, M. A. Gusinow and M. K. Matzen, Bull. Am. Phys. Soc. **23**, 777 (1978).

30. B. H. Ripin, J. M. McMahon, E. A. McLean, W. M. Manheimer, and J. A. Stamper, Phys. Rev. Lett. **33**, 634 (1974).

31. F. C. Young in NRL Memo No. 3591 (1977) (ed. S. Bodner).

32. N. G. Basov, V. A. Boiko, S. M. Zakharov, O. N. Krokin, G. V. Sklizkov and A. Y. Faenov, Sov. J. Quant. Electron. **3**, 444 (1974).

33. K. G. Tirsell, G. R. Tripp, E. M. Lent, R. A. Lerche, J. C. Chang, L. Hocker and P. B. Lyons, IEEE Trans. Nucl. Sci., **NS-24**, 250 (1977).

34. Similar hot spots were observed above 10^{14} W/cm^2 in x-ray pinhole photos taken of the front side of a target in: H. D. Shay, R. A. Haas, W. L. Kruer, M. J. Boyle, D. W. Phillion, V. C. Rupert, H. N. Kornblum, F. Rainer, V. W. Slivinsky, L. N. Koppel, L. Richards and K. G. Tirsell, Phys. Fluids **21**, 1634 (1978).

35. D. L. Blizzard (unpublished).

36. D. J. Nagel, P. G. Burkhalter, R. D. Bleach and D. L. Blizzard, Bull. Am. Phys. Soc. **23**, 803 (1978); D. J. Nagel and P. G. Burkhalter (to be published).

37. R. Resnick and D. Halliday, "Physics," Vol. I, pg. 178, J. Wiley NY (1978).

38. F. S. Felber, Phys. Rev. Lett. **39**, 84 (1977).

39. F. S. Felber, Nucl. Fusion **18**, 1469 (1978).

40. Some ablation models which attempt to include these effects are: Ref. 20, S. J. Gitomer, R. L. Morse, and B. S. Newberger, Phys. Fluids **20**, 234 (1977); C. E. Max and C. F. McKee, Phys. Rev. Lett. **39**, 1336 (1977); R. E. Kidder, Nucl. Fusion **8**, 3 (1968); J. L. Bobin, Phys. Fluids **14**, 2341 (1971); P. Mulser and C. van Kessel, Phys. Rev. Lett. **38**, 902 (1977); J. Virmont, R. Pellat and P. Mora, Phys. Fluids **21**, 567 (1978); and R. L. McCrory and R. L. Morse, Phys. Rev. Lett. **38**, 544 (1977); K.A. Brueckner, P.M. Campbell and R.A. Grandey, Nuclear Fusion **15**, 471 (1975).

41. T. R. Jarboe, W. B. Kunkel, and A. F. Lietzke, Phys. Fluids **19**, 1501 (1976).

42. H. Azechi, S. Oda, K. Tanaka, T. Norimatsu, T. Sasaki, T. Yamanaka and C. Yamanaka, Phys. Rev. Lett **39**, 1144 (1977).

43. P. J. Moffa, J. H. Orens, and J. P. Boris, private communications.

DEPARTMENT OF THE NAVY

NAVAL RESEARCH LABORATORY
Washington, D.C. 20375

OFFICIAL BUSINESS
PENALTY FOR PRIVATE USE, $300
Third Class Mail

POSTAGE AND FEES PAID
DEPARTMENT OF THE NAVY
DoD-316